ISSN 2822-2881

Firat University Journal of Experimental and Computational Engineering

Volume: 1 Issues: 1 Year: 2022

www.fujece.firat.edu.tr

Firat University Journal of Experimental and Computational Engineering

Fırat Üniversitesi Deneysel ve Hesaplamalı Mühendislik Dergisi

Volume: 1 Issues: 1 Year: 2022

Firat University Journal of Experimental and Computational Engineering

Fırat Üniversitesi Deneysel ve Hesaplamalı Mühendislik Dergisi

Volume: 1 Issues: 1 Year: 2022

Correspondence Address

Firat University Faculty of Engineering Journal of Experimental and Computational Engineering Publishing Coordinatorship

23119 Elazığ/TÜRKİYE

E-mail: fujece@firat.edu.tr

Web page: http://fujece.firat.edu.tr/

Firat University Journal of Experimental and Computational Engineering a peer-reviewed journal.

Firat University Journal of Experimental and Computational Engineering

Fırat Üniversitesi Deneysel ve Hesaplamalı Mühendislik Dergisi

Volume: 1 Issues: 1 Year: 2022

CONTENTS

Firat Univ Jour. of Exp. and Comp. Eng., 1(1), 1-7, 2022

Firat University Journal of Experimental and Computational Engineering
Fırat Üniversitesi Deneysel ve Hesaplamalı Mühendislik Dergisi

Effect of layer number on bending behavior of 3D spacer composite plates produced with different methods

Farklı yöntemlerle üretilen 3B boşluklu kompozit plakaların tabaka sayısının eğilme davranışına etkisi

Serkan ERDEM[1*], Mete Onur KAMAN[2], Mustafa GÜR[3]

[1,2,3] Department of Mechanical Engineering, Engineering Faculty, Firat University, Elazig, Turkey.
[1]serdem@firat.edu.tr, [2]mkaman@firat.edu.tr, [3]mgur@firat.edu.tr

Received: 17.12.2021
Accepted: 20.01.2022
Revision: 13.01.2022
doi: 10.5505/fujece.2022.10820
Research Article

Abstract
In this study, the three-point bending behavior of laminated composite plates reinforced with three-dimensional (3D) spacer fabric was experimentally investigated. Composite plate production was carried out using hand lay-up and vacuum infusion (VARI) method. Three-point bending test results of composite plates produced as a single layer were experimentally compared. Afterwards, composite plates with 2 and 3 layers were obtained by vacuum infusion method and load displacement graphs were obtained by subjecting them to three-point bending test. There was no significant difference between the load carrying capacities of the single-layer composite plates produced by hand lay-up and vacuum infusion method in the three-point bending test. According to the three-point bending test, the maximum load obtained 105 N in hand lay-up production is 8% greater than the vacuum infusion method. While the maximum load was 602 N in the plate produced in the 2-layer vacuum infusion method, it was obtained as 923 N in the 3-layer.

Keywords: 3D spacer composites, Three-point bending, Glass fiber, Vacuum infusion, Failure load.

Özet
Bu çalışmada, üç boyutlu (3B) boşluklu kumaş ile güçlendirilmiş tabakalı lamine kompozit plakların üç nokta eğilme davranışı deneysel olarak incelenmiştir. Kompozit plak üretimi elle yatırma ve vakum infüzyon yöntemi kullanılarak gerçekleştirilmiştir. Tek tabakalı olarak üretilen kompozit plakların Üç nokta eğilme test sonuçları deneysel olarak karşılaştırılmıştır. Sonrasında vakum infüzyon yöntemiyle 2 ve 3 tabakalı olarak kompozit plak elde edilmiş ve bunlar üç nokta eğilme testine tabi tutularak yük yer değiştirme grafikleri elde edilmiştir. Elle ve vakum infüzyon yöntemiyle üretilen tek tabakalı kompozit plakların üç nokta eğilme testinde yük taşıma kapasiteleri arasında kayda değer bir fark bulunmamıştır. Üç nokta eğme testine göre elle yatırmalı üretimde 105 N elde edilen maksimum yük, vakumlu infüzyon yöntemine göre %8 daha fazladır. 2 katmanlı vakum infüzyon yönteminde üretilen plakada maksimum yük 602 N iken, 3 katmanlıda 923 N olarak elde edilmiştir.

Anahtar kelimeler: 3 boyutlu boşluklu kompozitler, Üç nokta eğilme, Cam fiber, Vakum infüzyon, Hasar yükü.

1. Introduction

In order to increase the strength of the materials used in the construction, their thickness should be increased. However, doing this causes the weight of the materials to increase. The increase in weight causes an increase in energy costs in cases such as the production or transportation of materials. This situation contributes not only economically but also to global warming. Therefore, increasing the strength without increasing the thickness necessitates the addition of core material between the materials. The materials created in this type are called sandwich materials. Anything desired can be used as core material. Sandwich structure can be obtained by placing core material between composite materials. However, in these cases, there may be adhesion problems between the composite and the core material. Spacer fabrics are 3D sandwich fabric which are fabric at the bottom and top and fiber as the core.

*Corresponding author

Considering this advantage of spacer fabrics, many studies have been carried out. When the studies are examined: Green et al. calculated stress-strain under tensile loading for a 3D woven composite using the voxel method and damage analysis in finite element analysis. The aim of the study is to compare the idealized geometry with the real geometry by simulation. Simulated geometry models produced results close to experiments [1]. Neje et al. have produced woven spacer fabrics with different cell geometries such as rectangular, trapezoidal and triangular. Sandwich composite plates were produced from these fabrics by vacuum infusion method. The produced sandwich composites were analyzed for their quasi-static lateral compression and bending performances [2]. Safari et al. have created new hybrid composites by filling the channels of porous composites with polymer nanocomposite. Natural zeolite/polyurethane was used as nanocomposite. Flat compression, edge compression, three-point bending and weight drop tests were applied to measure the mechanical response of the samples. It has been obtained that zeolite particles significantly improves the mechanical properties of the filled composite sandwich panels [3]. Sadighi et al. investigated the mechanical behavior of 3D woven glass fiber sandwich composites experimentally and by the finite element method. Flat directional pressure, edge directional pressure, shear and three-point bending tests were performed for three different core thicknesses of sandwich panels. Consistency was obtained in the experimental studies with the studies carried out with the finite element method [4]. Zhang et al. investigated the effect of surface layer structure on 3D woven spacer composites. The effect of flat and complex surface layer on 3D woven spacer composites was investigated by three-point bending, quasi-static compression and low-speed impact tests [5]. Li et al have produced 3D spacer woven composites with thickened face layers. The effect of thickened surface layers was investigated by static compression and impact tests. Tests have shown that the face layer is an important parameter. The thickened face layers significantly improved the warp compression and impact properties [6]. Li et al. produced composites with thickened surface layers with 3D spacer woven fabric with the VARI process. Three-point bending test and fracture mechanism were analyzed to evaluate the effect of the thickened surface plates. It has been reported that the surface plate thickness is a parameter that affects the mechanical properties of the 3D spacer woven composite [7]. Umair et al. produced composites by hand lay-up technique using 3D spacer woven E-glass fabric with three thickness levels (4, 10 and 20 mm) as fiber and epoxy resin as matrix. The stiffness of the fabric increased as the sample thickness increased, and the bending modulus decreased as the length of the 3D spacer woven fabrics increased. As the sample thickness increased, the bending and slow velocity impact strength of the 3D spacer woven composites decreased [8]. Wang et al. produced composites using 3D spacer glass woven fabric as fiber and epoxy resin as matrix. The produced composites exhibited excellent compressive strength as well as good thermal insulation [9]. Atar et al. [10] evaluated the effect of core geometry on bending stiffness and transverse shear stiffness in corrugated core sandwich panels experimentally and numerically. Three-dimensional composite sandwich panels with rectangular, trapezoidal and triangular cross-section geometries were produced. A significant relationship was found between the direction of corrugation and the load carrying capacity.

When the studies in the literature are examined, it is seen that the composite plates are produced only by hand lay-up or VARI technique [1-10] and the produced plates are obtained as a single 3D spacer layer. Unlike the literature in this study, the effect of these two production techniques on bending strength was investigated experimentally. In addition, multi-layer composite plate was produced with the VARI method, and the effect of the increase in the number of layers on the increase in bending behavior was investigated. Obtained strength behavior for three-point bending test were presented in graphic form.

2. Material and Method

In this study, composite plates were produced using 3D spacer glass fiber fabrics (Figure 1). Composite plate production was carried out by hand lay-up and VARI method. While 3D spacer glass fabric was used as fiber, F-1564 resin and F-3487 hardener set purchased from Fibermak Composites Izmir, Turkey were used as matrix. The mixing ratio of resin and hardener is 100:34 respectively. 800 g matrix and 1 m^2 fabric were used.

2.1. Hand lay-up method

The spacer glass fiber fabric was laid on the bench floor and the resin, hardener mixture was applied to the fabric manually with the help of a roller. The fabric was left to dry for 24 hours at room temperature. Then, the test samples were cut from the composite plate in accordance with ASTM D790 [11] standards by marble cutting machine.

2.2. VARI method

Each step of the VARI production steps was applied sequentially [12-13]. The production is based on the principle that the resin is given on the one hand and the fabric is wetted on the other hand. In vacuum infusion; The resin is given to the system under the effect of vacuum and left to wait under the same vacuum. Sandwich structure cannot be obtained because the lower and upper face sheets of 3D spacer fabrics will stick together due to vacuum and the wall thickness of the obtained composite plates will decrease. However, in this study, primarily a sandwich structure was desired, so resin was injected into the system and the entire fabric was wetted (Figure 2a).

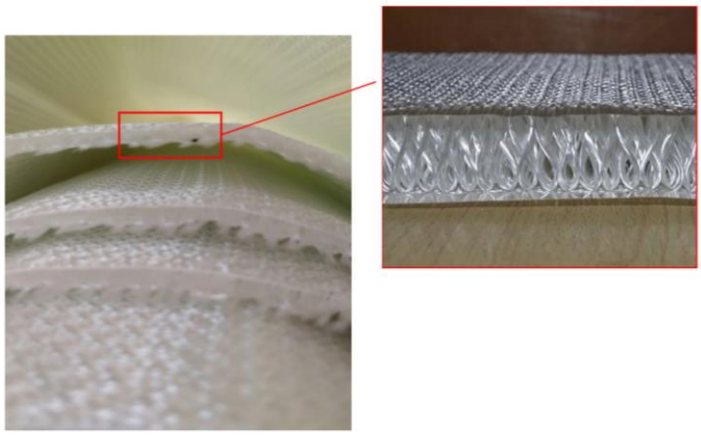

Figure 1. 3D spacer glass fabrics used for composite plate production

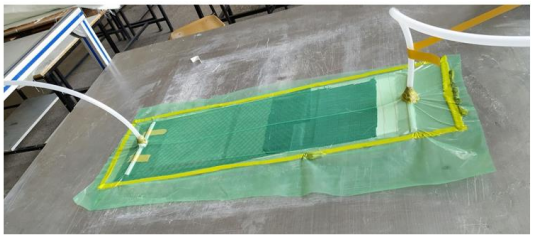

a)

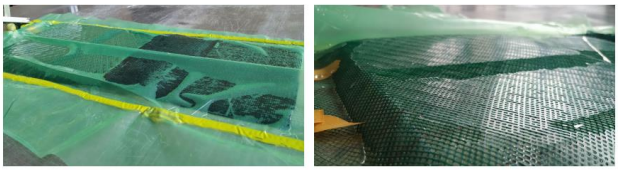

b)

Figure 2. Production of composite plates using VARI method a) the vacuum applying, b) removing the vacuum and drying

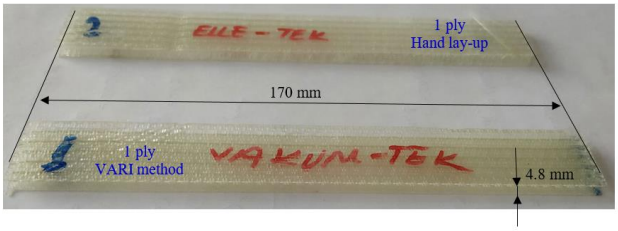

Figure 3. Thicknesses of one layer specimens produced with hand lay-up and VARI method

Then, the vacuum was removed and the fabrics were stretched to rise back and formed a sandwich structure (Figure 2b). In vacuum infusion production, the vacuum was turned off when the process of giving resin to the fabric was finished. This time is approximately two minutes. At the end of the vacuum process, the fabric has become 3D by itself. The thickness of the composite plates produced as a single layer was obtained as 4.8 mm in both methods. Experiment samples were obtained from the produced composite plates according to ASTM D790 standards by using marble cutting machine (Figure 3). In the production of multi-layer composites, dry fabrics were placed on top of each other and then the vacuum infusion production steps explained above were repeated. Resin-impregnated fabrics were cut into desired dimensions after waiting for 24 hours at room temperature. After fabrication, the total thicknesses of the 2- and 3-layer composite plates were measured as 9.2 mm and 13.6 mm, respectively. Three-point bending tests were carried out one week after production.

2.3. Three-point bending test

Three-point bending test of 3D composite plates produced by hand lay-up and vacuum infusion method and cut in ASTM D790 standard was performed at 0.5 mm/min speed on Utest 10 kN tensile device (Figure 4). The dimensions of all specimens are 25x170 mm. The thicknesses are 4.8 mm (Figure 3).

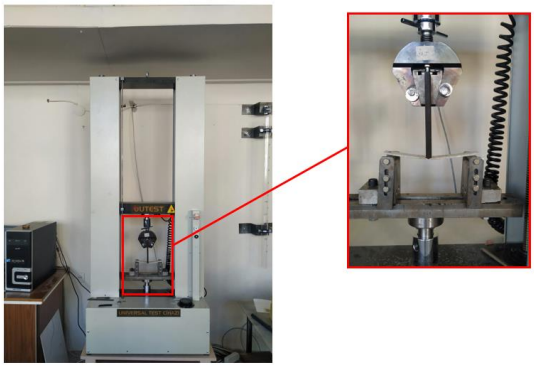

Figure 4. Universal tension test machine and three-point bending test setup

3. Results and Discussions

Load displacement graphs were obtained from the three-point bending test results of composite plates produced from 3D spacer glass fiber fabric by hand lay-up and vacuum infusion method. In addition, the maximum bending strength was also determined.

3.1. Hand lay-up method

Three-point bending result graph of the composite plate produced as a single layer from 3D spacer glass fiber is shown in Figure 5. In Figure 5, the maximum load of 108.61 N and a displacement of 0.463 mm were obtained in the load-displacement graph. It has been observed that the relationship between load and displacement is linear. This indicates that the material behaves brittle. After the maximum load, there was a sudden drop in load.

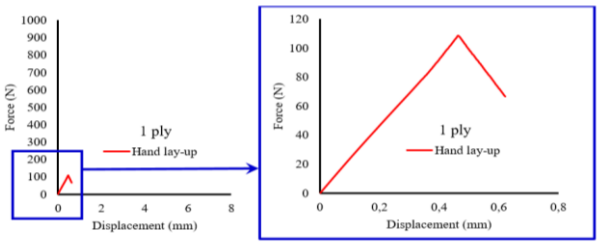

Figure 5. Force-displacement graph of one-layer composite sandwich produced with hand lay-up

3.2. VARI method

The load-displacement behaviors of composite plates produced from 3D spacer glass fiber fabric as single, double and triple layers were obtained as shown in Figure 6. The load-displacement behavior of the composite plate produced with VARI method as a single layer is linear [14]. This behavior is similar to that of plates produced by the hand lay-up method. The bending behavior of two- and three-layer composites is non-linear, unlike single-layer composites. Depending on the manufacture, the height of each layer may not be the same. For this reason, the resistance of each layer to bending will be slightly different. Therefore, partial deviations from linearity are seen in the graphs up to the maximum load. However, sudden but partial decreases in load are seen in the graph of multi-layer composites. During bending, shear stresses will arise between the layers. This will force the matrix holding the layers together to suffer damage. Therefore, regional delamination damage may occur between layers. Karahan et al. stated that damages occurred on foam-filled 3D spacer composite samples as extra skin-core delamination [15]. Another damage behavior is regional core crushing on the load applied surfaces. Since the load-displacement behavior is linear in monolayer composites, such damage also determines the bending stiffness of the plate. However, in multi-layer composites, the first layer is crushed first at the load contact point [8, 16-17]. Then the second layer is broken. In the triple layer, fracture occurs in the last layer. This causes a gradual decrease in the load.

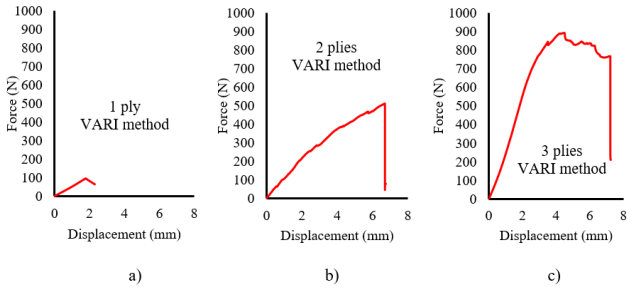

Figure 6. Force displacement graph of composite plate consisted of a) one ply, b) two plies and c) three plies

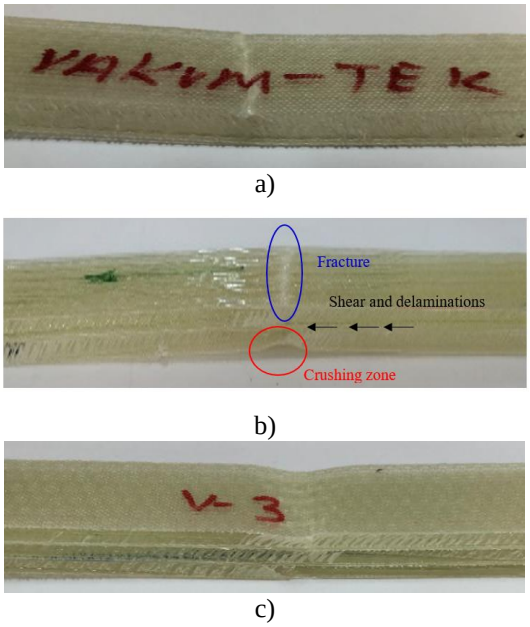

Figure 7. Failure mechanisms of composite plate consisted a) one, b) two and c) three plies

Maximum damage loads of single-layer composite plates produced by hand lay-up and vacuum infusion method and two- and three-layer composite plates produced by vacuum infusion method are presented in Figure 8. According to the three-point bending chart, the maximum load obtained 105 N in hand lay-up production is 8% greater than the vacuum infusion

method. Manufacturing the composite plate by hand lay-up or by vacuum infusion method had limited effect in terms of maximum load. While the maximum load was 602 N in the plate produced in the 2-layer vacuum infusion method, it was obtained as 923 N in the 3-layer.

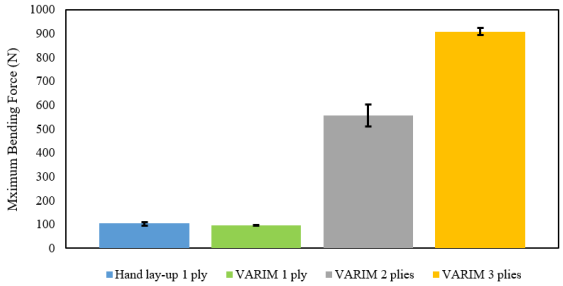

Figure 8. Variation of maximum bending forces with layer number and production method

4. Conclusion

In this study, 3D spacer glass fiber reinforced composite plates were produced using hand lay-up and VARI method. The results obtained as a result of the three-point bending test can be summarized as follows.

• Different production methods used for monolayer composites changed the bending stiffness by 8%. This shows that the production method does not have a significant effect on the bending stiffness.

• The increase in the number of layers increased the bending load. A strength increase of ~600% was obtained when two layers were used, and ~900% when three layers were used.

• The bending behavior of the monolayer composite is linear. However, the bending behavior of two- and three-layer composites is non-linear. In addition, partial load drops have occurred due to sheet crushing and delamination at the load contact point.

5. Author Contribution Statement

In the study, Author 1 contributed making the design and literature review; Author 2 contributed to forming the idea, the analysis of the results, provision of the materials and examination of the results; Author 3 contributed to checking the spelling and checking the article in terms of content.

6. Ethics Committee Approval and Conflict of Interest

There is no need for an ethics committee approval in the prepared article. There is no conflict of interest with any person/institution in the prepared article.

7. References

[1] Green SD, Matveev MY, Long AC, Hallett SR. "Mechanical modelling of 3D woven composites considering realistic unit cell geometry". *Composite Structures*, 118, 284-293, 2014.

[2] Neje G, Behera BK. "Investigation of mechanical performance of 3D woven spacer sandwich composites with different cell geometries". *Composites Part B*, 160, 306–314, 2019.

[3] Safari H, Karevan M, Nahvi H. "Mechanical characterization of natural nano-structured zeolite/polyurethane filled 3D woven glass fiber composite sandwich panels". *Polymer Testing*, 67, 284–294, 2018.

[4] Sadighi M, Hosseini SA. "Finite element simulation and experimental study on mechanical behavior of 3D woven glass fiber composite sandwich panels". *Composites: Part B*, 55, 158–166, 2013.

[5] Zhang M, Wang X, Liu S, Li F, Wu G. "Effects of Face Sheet Structure on Mechanical Properties of 3D Integrated Woven Spacer Composites". *Fibers and Polymers*, 21(7), 1594–1604, 2020.

[6] Li DS, Jiang N, Jiang L, Zhao CQ. "Static and dynamic mechanical behavior of 3D integrated woven spacer composites with thickened face sheets". *Fibers and Polymers*, 17(3), 460–468, 2016.
[7] Li DS, Zhao CQ, Jiang N, Jiang L. "Fabrication, properties and failure of 3D integrated woven spacer composites with thickened face sheets". *Materials Letters*, 148, 103–105, 2015.
[8] Umair M, Hamdani STA, Nawab Y, Asghar MA, Hussain T, Saouab A. "Effect of Pile Height on the Mechanical Properties of 3D Woven Spacer Composites". *Fibers and Polymers*, 20(6), 1258–1265, 2019.
[9] Wang L, Zhang K, Farha FI, Ma H, Qiu Y, Xu F. "Compressive strength and thermal insulation properties of the 3D woven spacer composites with connected spacer yarn structure". *Journal of Materials Science,* 55(6), 2380–2388, 2020.
[10] Atar HA, Zarrebini M, Hasani H, Rezaeepazhand J. "The effect of core geometry on flexural stiffness and transverse shear rigidity of weight-wise identical corrugated core sandwich panels reinforced with 3D flat spacer knitted fabric". *Polymer Composites,* 41(9), 3638–3648, 2020.
[11] Masoumi M, Mansoori H, Dastan T, Sheikhzadeh M. "An experimental investigation into flexural properties of hybrid carbon-basalt triaxially braided composite lamina". *Composite Structures*, 284, 115231, 2022
[12] Erdem S, Gur M, Kaman MO. "Nonlinear buckling behavior of hybrid composites with different notch types". *Materials Testing*, 63(9), 797–804, 2021.
[13] Erdem S, Gur M, Kaman MO. "Effect of patch dimension and fiber orientation on non-linear buckling of hybrid composites". *Materials Testing*, 63(10), 929–942, 2021.
[14] Li M, Wang S, Zhang Z, Wu B. "Effect of structure on the mechanical behaviors of three-dimensional spacer fabric composites". *Applied Composite Materials*, 16(1), 1–14, 2009.
[15] Karahan M, Gul H, Karahan N, Ivens J. "Static behavior of three-dimensional Integrated core sandwich composites subjected to three-point bending". *Journal of Reinforced Plastics and Composites*, 32(9), 664–678, 2013.
[16] Hassanzadeh S, Hasani H, Zarrebini M. "Mechanical characterization of innovative 3D multi-cell thermoset composites produced with weft-knitted spacer fabrics". *Composite Structures*, 184, 935-949, 2018.
[17] Hamedi S, Hasani H, Dibajian SH. "Numerical simulating the flexural properties of 3D weft-knitted spacer fabric reinforced composites". *Journal of composite materials,* 51(13), 1887–1899, 2017.

Firat Univ Jour. of Exp. and Comp. Eng., 1(1), 8-13, 2022

Firat University Journal of Experimental and Computational Engineering
Fırat Üniversitesi Deneysel ve Hesaplamalı Mühendislik Dergisi

The use of mixed algae species as biocathode in membrane-less microbial fuel cell

Karışık alg türlerinin membransız mikrobiyal yakıt hücresinde biyokatot olarak kullanımı

Banu TAŞKAN[1*]

[1]Environmental Engineering, Engineering Faculty, Firat University, Elazig, Turkey.
[1]btaskan@firat.edu.tr

Received: 14.01.2022
Accepted: 05.02.2022
Revision: 01.02.2022
doi: 10.5505/fujece.2022.18209
Research Article

Abstract
Membrane-less microbial fuel cell (MLMFC) is one of the most promising technologies for energy generation from organic wastes. The use of biocathode in the MLMFC system reduces the operation cost and provides many benefits. In an algal MLMFC system, the photosynthetic microorganism facilitates the oxygen reduction in the cathode chamber and improves overall cell performance. However, the assessment of the long-term stability of biocathode is a primary concern. In the current study, the electricity generation performance of algal MLMFC using mixed-algae as a biocathode was investigated. The results showed that the electricity generation of algal MLMFC increased during the light cycle because of the photosynthesis of algal cells in the cathode. During the light cycle, the maximum power density and lowest cathode charge transfer resistance of algal MLMFC were 215.71 mW/m^2 and 29.73 Ω, respectively. The electrochemical analysis demonstrated that the anode biofilm of algal MLMFC has high bioelectrogenic activity. This study plays a crucial role in determining the applicability of this technology.

Keywords: Membrane-less microbial fuel cell, Biocathode, Mixed algae, Power density.

Özet
Membransız mikrobiyal yakıt hücresi (MMYH), organik atıklardan enerji üretimi için en umut verici teknolojilerden biridir. MMYH sisteminde biyokatot kullanımı işletme maliyetini düşürür ve birçok fayda sağlar. Algal bir MMYH sisteminde, fotosentetik mikroorganizma, katot bölümünde oksijen azalmasını kolaylaştırır ve genel hücre performansını iyileştirir. Bununla birlikte, biyokatodun uzun vadeli stabilitesinin değerlendirilmesi birincil endişe kaynağıdır. Mevcut çalışmada, biyokatot olarak karışık alg kullanan algal MMYH'nin elektrik üretim performansı araştırılmıştır. Sonuçlar, katottaki alg hücrelerinin fotosentezi nedeniyle ışık döngüsü sırasında algal MMYH'nin elektrik üretiminin arttığını gösterdi. Işık döngüsü sırasında, algal MMYH'nin maksimum güç yoğunluğu ve en düşük katot transfer direnci sırası ile 215.71 mW/m^2 ve 29.73 Ω idi. Elektrokimyasal analiz, algal MMYH'nin anot biyofilminin yüksek biyoelektrojenik aktiviteye sahip olduğunu göstermiştir. Bu çalışma, bu teknolojinin uygulanabilirliğinin belirlenmesinde çok önemli bir rol oynamaktadır.

Anahtar kelimeler: Membransız mikrobiyal yakıt hücresi, Biyokatot, Karışık alg, Güç yoğunluğu.

1. Introduction

Microbial fuel cells (MFCs) are reactors that generate bioelectricity by converting chemical energy into electrical energy. [1]. MFCs can produce electricity and wastewater treatment simultaneously. In an MFC, the bacteria in the biofilm on the anode electrode produce electrons (e^-) by consuming organic wastes fed in anode and transfer to the anode electrode [2]. These electrons move to the cathode on the external resistance and are used by a reduction reaction [3]. The reduction of oxygen in the cathode can produce a theoretic open-circuit voltage of 1.16V [4]. However, the low cathode performance, energy loss, low electrode activity, and low oxygen transfer from the atmosphere to the cathode liquid limits cathode performance [5]. Different cathode catalysts are generally used to improve the cathode performance of MFCs to provide effective oxygen reduction in the cathode chamber. The platinum (Pt) is a commonly used catalyst used in the cathode of MFC, which has a substantial reduction activity to provide a high cathodic potential [6]. In some previous studies, the

*Corresponding author

$MnSO_4$, MnO_2, and catalysts of carbon nanotube-supported MnO_2 are cheaper than platinum, were used instead of platinum [7]. In addition to this, the cost and disposal of chemical catalysts still restrict the improvement of MFCs [8].

In addition to the use of chemical catalysts in the cathode of MFCs, the development of biocathodes has a significant potential for wastewater treatment and large-scale applications of the MFCs [9]. In particular, photosynthetic oxygen generation is quite interesting to provide oxygen as an electron acceptor and eliminate the energy requirement [10]. Recent studies using pure culture as biocathode suggest that the electron transfer mechanism of various strains could be critical. [8, 11]. Many algae species have been used as biocathode in MFCs, such as *Scenedesmus acutus* [12], *Chlorella vulgaris* [10], *Chlorella* sp. [13]. Although the previous studies demonstrated the increase in cathode performance of MFCs using photosynthetic microorganisms, the implementation of the biocatalyzed biocathodes is still unclear, as many studies have been carried out for the short-term operation [8].

In this study, the mixed microalgae were used as biocathode in the cathode chamber of algal MLMFC. The performance of algal MLMFC was evaluated by electrochemical analysis and the concentration of DO measurement in the cathode chamber.

2. Material and Methods

2.1. Cultivation of mixed algae

The algal samples were collected from the Keban Lake (Elazig). It was then cultivated in a photobioreactor system described in our previous study using BG-11 medium [14]. The photobioreactor system was operated with 75 µmol photons/m^2s. The cultivated algal biomass was used in the cathode chamber of the MLMFC as a biocathode.

2.2. Construction of algal MLMFC and operation

The schematic diagram of the algal MLMFC system is shown in Figure 1. A cylindrical plastic container was used as the algal MLMFC reactor. The dimensions of the algal MLMFC were 7 cm in diameter and 18 cm in height. The platinum mesh and stainless steel mesh were used as cathode and anode electrodes [15].

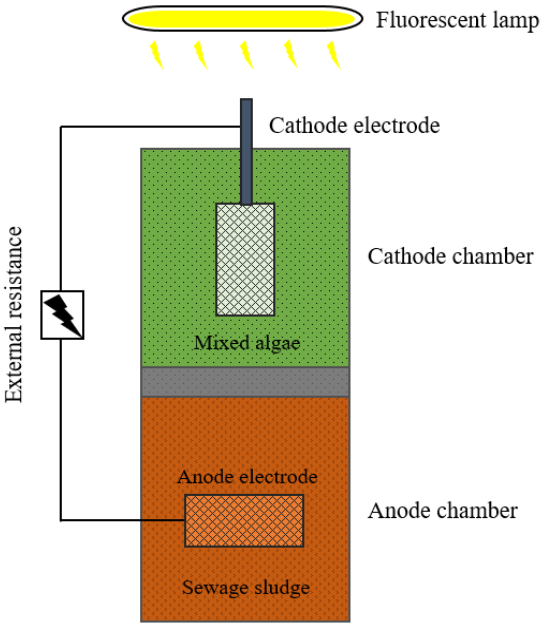

Figure 1. The schematic diagram of algal MLMFC

A sand layer of 3 cm was filled on the anode chamber to physically separate the cathode and anode chambers and prevent the transport of anode medium to the cathode chamber. The height of the anode and cathode chambers was 8 cm. The anode and cathode electrodes were fixed with an external resistance of 1000 Ω. The wastewater treatment sludge obtained from the Elazig municipal wastewater treatment plant was used as a substrate for anode microorganisms. The anode chamber was covered with an aluminum folio to prevent growing photosynthetic microorganisms in the anode chamber of algal MLMFC. The cathode chamber of algal MLMFC was illuminated with a light intensity of 60 μmol photon/m^2.s using a fluorescence lamp.

2.3. Analysis

The voltage of algal MLMFC was measured using 34970A digital multimeter (Data Acquisition/Switch Unit) and saved to the computer. The electrochemical analysis of algal MLMFC was carried out Gamry Interface 1000 potentiostat (Gamry, Warminster, PA). The electrochemical impedance spectroscopy (EIS) and linear sweep voltammetry (LSV) analysis were carried out described in Taşkan [16]. The EIS data were fitted using a circuit model (Figure 4) given by Abazarian, et al. [13]. The concentration of dissolved oxygen (DO) was measured with a time interval of 15 min using a digital multimeter (Hach Lange HQ40D, Germany).

3. Results and Discussion

3.1. The DO concentration in the cathode

The algal cells produce oxygen under light conditions by photosynthesis, and they use the oxygen under dark conditions for respiration. Figure 2 shows the change in DO concentration in a day under dark and light conditions. It was determined that the maximum DO concentration of the cathode reached 14.79 mg/L at the end of the light period and significantly decreased with the turn of the fluorescence lamp. Kakarla and Min [12] reported a maximum DO concentration of 15.7 in the cathode of the biocathode MFC using *Scenedismus obliquus* in the cathode. Abazarian, et al. [13] reported a maximum oxygen concentration of 6.3 ± 0.1 mg/L in the cathode of MFC using mechanical aeration. The maximum DO concentration obtained in this study is more than two times the value obtained by Abazarian, et al. [13]. Additionally, a positive correlation between voltage and DO concentration was determined.

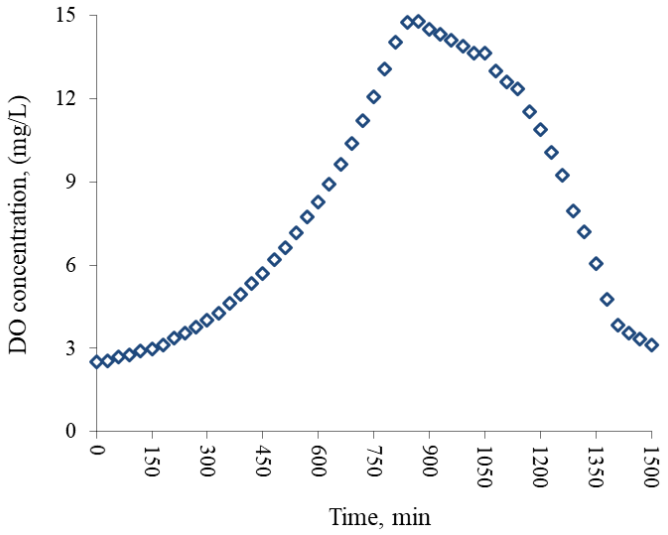

Figure 2. One-day DO concentration variation of the cathode chamber

3.2. Power density

Figure 3 shows the power curve of algal MLMFC. The maximum power density of the algal MLMFC was determined to be 215.71 mW/m^2. The maximum power density is relatively higher than literature values obtained by MFC with the algal cathode. The previous studies reported a positive correlation between power density and DO concertation in the cathode of MFC [17]. A maximum power density of 153 mW/m^2 was reported by a previous study, using *Scenedismus obliquus* in the cathode of MFC [12]. The obtained maximum power density of this study is higher than that obtained by Kakarla and Min [12]. In another study, the maximum power density produced by using *Chlorella* sp. as a photosynthetic biocathode in sediment-type MFC was reported to be 19.6 mW/m^2 [13].

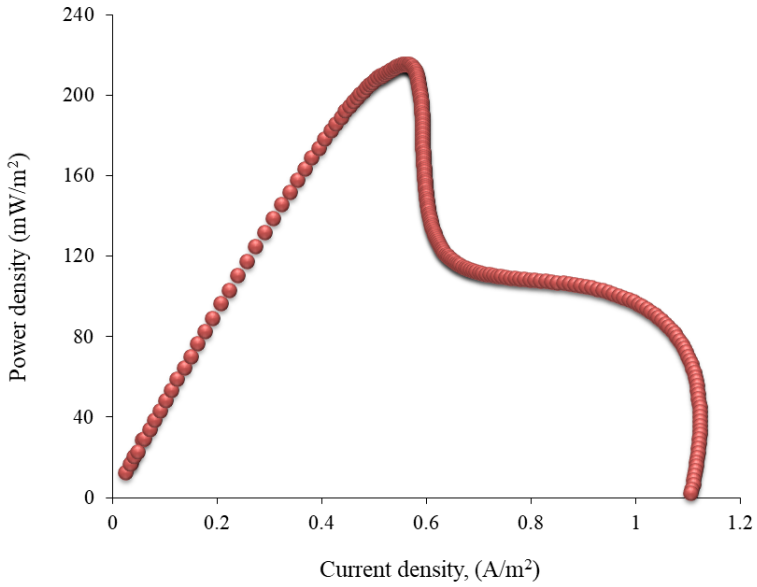

Figure 3. Power density curve

3.3. Electrochemical characterization of algal MLMFC

The circuit model and fitted EIS results are shown in Figure 4. The performance of cathodic oxygen reduction reactions in an MFC is relatively crucial to improving MFC's performance. The high DO concentration in the chamber of cathode promotes the electricity generation performance of MFC. The determination of constitution and distribution of internal resistance is required to increase MFC performance and obtain optimum power density [18, 19]. The performance of algal MLMFC can be increased by decreasing the components of internal resistance. The analysis of EIS was performed to investigate the components of the internal resistance of MFC. In the circuit model, R_{ct} is charge transfer resistance, R_{mt} is mass transfer resistance, R_s is solution resistance, R_o is other resistances in the cathode, and CPE is double-layer constant phase elements. The R_s and R_{ct} of the algal MLMFC were 51.55 Ω and 29.73 Ω. Consequently, biocathode in MFCs can make the distribution of electrons easy and improve the system performance incredibly.

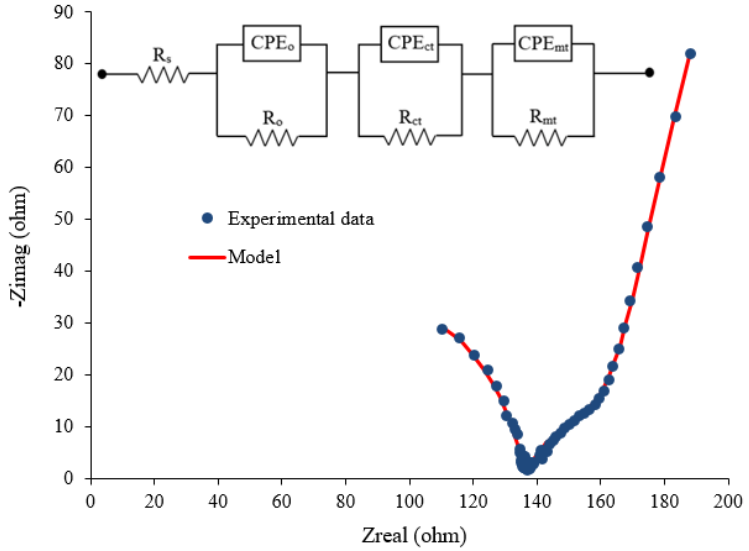

Figure 4. Equivalent circuit model and nyquist plot

4. Conclusion

The current study used the mixed algae culture as biocathode in algal MLMFC. The electricity generation performance of algal MLMFC was investigated in detail. The results showed that the dark and light periods are very effective on the performance of algal MLMFC. The performance of reactor increased during the light period. Algal MLMFC produced a high-power density of 215.71 mW/m^2. The results showed that the photosynthetic biocathode facilitates the oxygen reduction reaction at the cathode and the potential applicability of this technology.

5. Author Contribution Statement

In the study, Author 1 contributed (I) making the design and literature review, (ii) to form the idea, the analysis of the results, provision of the materials, and examination of the results, (iii) to checking the spelling and checking the article in terms of content.

6. Ethics Committee Approval and Conflict of Interest

There is no need for an ethics committee approval in the prepared article. There is no conflict of interest with any person/institution in the prepared article.

7. References

[1] Allen RM, Bennetto HP. "Microbial fuel-cells". *Applied Biochemistry and Biotechnology*, 39(1), 27-40, 1993.
[2] Bennetto H. "Electricity generation by microorganisms". *Biotechnology education*, 1(4), 163-168, 1990.
[3] Rabaey K, Ossieur W, Verhaege M, Verstraete W. "Continuous microbial fuel cells convert carbohydratesto electricity". *Water Science and Technology*, 52(1-2), 515-523, 2005.
[4] Nørskov JK, Rossmeisl J, Logadottir A, Lindqvist L, Kitchin JR, Bligaard T, Jónsson H. "Origin of the overpotential for oxygen reduction at a fuel-cell cathode". *The Journal of Physical Chemistry B*, 108(46), 17886-17892, 2004.
[5] Gewirth AA, Thorum MS. "Electroreduction of dioxygen for fuel-cell applications: materials and challenges". *Inorganic Chemistry*, 49(8), 3557-3566, 2010.
[6] Cheng S, Liu H, Logan BE. "Power densities using different cathode catalysts (Pt and CoTMPP) and polymer binders (Nafion and PTFE) in single chamber microbial fuel cells". *Environmental Science & Technology*, 40(1), 364-369, 2006.
[7] Lu M, Kharkwal S, Ng HY, Li SFY. "Carbon nanotube supported MnO_2 catalysts for oxygen reduction reaction and their applications in microbial fuel cells". *Biosensors and Bioelectronics*, 26(12), 4728-4732, 2011.

[8] Chang CC, Li SL, Hu A, Yu CP. "Long-term operation of bio-catalyzed cathodes within continuous flow membrane-less microbial fuel cells". *Chemosphere*, 266, 129059, 2021.
[9] Huang L, Regan JM, Quan X. "Electron transfer mechanisms, new applications, and performance of biocathode microbial fuel cells". *Bioresource Technology*, 102(1), 316-323, 2011.
[10] del Campo AG, Perez JF, Cañizares P, Rodrigo MA, Fernandez FJ, Lobato J. "Characterization of light/dark cycle and long-term performance test in a photosynthetic microbial fuel cell". *Fuel*, 140, 209-216, 2015.
[11] Liu H, Matsuda S, Hashimoto K, Nakanishi S. "Flavins secreted by bacterial cells of Shewanella catalyze cathodic oxygen reduction". *ChemSusChem*, 5(6), 1054-1058, 2012.
[12] Kakarla R, Min B. "Photoautotrophic microalgae Scenedesmus obliquus attached on a cathode as oxygen producers for microbial fuel cell (MFC) operation". *International Journal of Hydrogen Energy*, 39(19), 10275-10283, 2014.
[13] Abazarian E, Gheshlaghi R, Mahdavi MA. "Impact of light/dark cycle on electrical and electrochemical characteristics of algal cathode sediment microbial fuel cells". *Journal of Power Sources*, 475, 228686, 2020.
[14] Güneş G, Taşkan E. "Quorum quenching strategy for biofouling control in membrane photobioreactor". *Chemosphere*, 288, 132667, 2022.
[15] The Fuel Cell Store. "The Fuel Cell Store". https://www.fuelcellstore.com/ (24.02.2022).
[16] Taşkan B. "Increased power generation from a new sandwich-type microbial fuel cell (ST-MFC) with a membrane-aerated cathode". *Biomass and Bioenergy*, 142, 105781, 2020.
[17] Rismani-Yazdi H, Carver SM, Christy AD, Tuovinen OH. "Cathodic limitations in microbial fuel cells: an overview". *Journal of Power Sources*, 180(2), 683-694, 2008.
[18] Kashyap D, Dwivedi PK, Pandey JK, Kim YH, Kim GM, Sharma A, Goel S. "Application of electrochemical impedance spectroscopy in bio-fuel cell characterization: A review". *International Journal of Hydrogen Energy*, 39(35), 20159-20170, 2014.
[19] Fan Y, Sharbrough E, Liu H. "Quantification of the Internal Resistance Distribution of Microbial Fuel Cells". *Environmental Science & Technology*, 42(21), 8101-8107, 2008.

Firat Univ Jour. of Exp. and Comp. Eng., 1(1), 14-23, 2022

Firat University Journal of Experimental and Computational Engineering
Fırat Üniversitesi Deneysel ve Hesaplamalı Mühendislik Dergisi

Modeling of a solar air collector heat transfer coefficient with regression algorithms

Bir havalı güneş kollektörü ısı transfer katsayısının regresyon algoritmaları ile modellenmesi

Ebru Kavak AKPINAR[1]*, Mehmet DAŞ [2]

[1]Department of Mechanical Engineering, Faculty of Engineering, Firat University, Elaziğ, Turkiye.
[2]Department of Mechanical Engineering, Faculty of Architecture and Engineering, Tokat Gaziosmanpasa University, Tokat, Turkiye.
[1]ebruakpinar@firat.edu.tr, [2]mehmet.das@gop.edu.tr

Received: 31.12.2021
Accepted: 07.02.2022
Revision: 28.01.2022
doi: 10.5505/fujece.2022.43153
Research Article

Abstract
Solar air collectors (SAC) are thermodynamic systems that convert solar energy into useful fluid energy. SACs are very common in heating, cooling, food drying, and many other low-temperature applications. In this study, the heat transfer coefficient in the SAC was calculated according to Newton's cooling law. The obtained values and the thermal performance of the SAC were examined during the sunshine period. At the same time, SAC heat transfer coefficient models were made with the help of regression algorithms (multiple linear regression, simple linear regression) using SAC temperature data obtained by experimental measurements (inlet fluid, outlet fluid, and absorber plate) and solar radiation data on the SAC. As a result of the modeling, linear mathematical equations expressing the heat transfer coefficient for SACs were obtained. Obtained experimental and model data were compared. SAC heat transfer coefficient values were modeled with a mean absolute error of 0.6.

Keywords: Solar air collector, Heat transfer coefficient, Solar energy, Regression, Equation derivation

Özet
Havalı güneş kollektörleri (HGK), güneş enerjisini faydalı akışkan enerjisine dönüştüren termodinamik sistemlerdir. Isıtmada, soğutmada, gıda kurutmada ve daha birçok düşük sıcaklık uygulamalarında HGK'ların kullanımı oldukça yaygındır. Bu çalışmada HGK içerisindeki ısı transfer katsayısı Newton soğutma kanununa göre hesaplanmış ve elde edilen değerler ile HGK'nın termal performansı güneşlenme süresi boyunca incelenmiştir. Aynı zamanda deneysel ölçümler ile elde edilen HGK sıcaklık verileri (giriş akışkan, çıkış akışkan ve yutucu plaka) ve kollektör üzerine gelen güneş radyasyon verileri kullanılarak regresyon algoritmaları (çoklu liner regresyon, basit liner regresyon) yardımıyla HGK ısı transfer katsayısı modellemeleri yapılmıştır. Modellemeler sonucu HGK lar için ısı transferi katsayısını ifade eden doğrusal matematiksel eşitlikler elde edilmiştir. Elde edilen deneysel ve model verileri karşılaştırılmıştır. HGK ısı transferi katsayısı değerleri 0.6 ortalama mutlak hata değeri ile modellenmiştir.

Anahtar kelimeler: Havalı güneş kollektörü, Isı transfer katsayısı, Güneş enerjisi, Regresyon, Eşitlik üretme

1. Introduction

One of the most important components of solar energy systems is undoubtedly flat plate type solar collectors. Solar collectors are system elements that collect the usable energy from the sun and transmit it to another environment using various fluids [1]. Among flat plate type solar collectors, the usage areas of SAC type collectors are pretty comprehensive. The SACs, which are used primarily in food drying [2,3] and space heating [4], are preferred as an alternative energy method due to the gradual depletion of fossil fuels and the harmful environmental effects of fuels [5]. The working principle of SACs is quite simple. When the sun's rays come to the SAC collector absorber surface, the absorber plate heats up, and this heat is transferred to the air passing over the plate, thereby heating the collector outlet air [6]. In the SACs, there is a heat transfer between the absorber plate and the fluid, and this heat transfer takes place by convection heat transfer (h) according to Newton's cooling law [7,8].
Many data are obtained as a result of experimental studies. Various calculations and models are created with this data. Models produced with experimental data are a structure that allows the data to be observed better. A model with a

*Corresponding author

theoretical framework helps to understand a particular phenomenon better. The linear model is of primary importance in the education of any theoretical or applied mathematician. Linear statistical models are widely used in engineering and other science fields as part of these processes [9]. There are many studies in the literature modeling the thermal efficiency of SAC with MLR [10-13]. When these studies are examined, there are temperature and radiation values in the data set created to model SAC thermal efficiency.

In this study, the heat transfer coefficient of SAC was calculated using experimental data. The data set used in the calculations was also modeled with regression algorithms, and mathematical equations were produced for the h values. Linear mathematical equations expressing two h values were obtained with multiple and simple regression algorithms. The h values obtained by the models were compared with the experimental h values. The regression equation that best expresses the h coefficient used for the heat transfer in SAC was determined.

2. Materials and Methot

The dimensions of the SAC used in the experiments are 1400mm x 800 x 150mm. The SAC structure consists of a transparent cover, absorber plate, flat plate, insulation layer, and outer casing. The SAC consists of 12 mm thick tempered glass as transparent cover and 0.5 mm thick matt-black painted corrugated stainless-steel sheet as absorber plate. In SAC, 4 cm thick rock wool was used as insulation material, and 4 mm thick aluminum was used as outer casing material. A radial fan (0.15 m^3/h, 0.18 kW, 220 V, 50 Hz, 2800 rpm) connected to the air inlet parts of the SAC with a hood provided the necessary air. The materials and properties of the SAC system are given in Table 1. The view of the experimental setup is shown in Figure 1.

The measurements were carried out in June 2018 under the climatic conditions of Elazig province. In the experiments, collector inlet temperature, collector outlet temperature, panel glass temperature, panel ground temperature, and solar radiation values were measured at intervals of 30 minutes. Waterproof DS18B20 digital temperature sensors and pyranometer are used for these measuring points. The experiments were carried out at a constant air velocity of 0.18 m/s and a constant mass airflow rate of 0.023 kg/s. The experiments carried out on 1-2 June were started at 08:00 and ended at 18:00.

J type iron-constantan thermocouples, manually controlled 20-channel automatic digital thermometer (ELIMKO, 6400) in the measurements of collector inlet temperature (T_i), collector outlet temperature (T_o), collector absorber plate temperature (T_{yp}), collector ground temperature (T_{ta}) with a reading accuracy of ±0.1 °C. Collector outlet air velocity was measured with a 0–15 m/s digital anemometer (LUTRON, AM-4201) with a reading accuracy of ± 0.01 m/s. While the system was operating, the solar radiation was measured with a sensitivity of ± 0.1 W/m^2 and a Kipp and Zonen pyranometer in a CC12 model digital solar integrator. Collector measurement points are shown schematically in Figure 2.

Figure 1. Front (1) and rear (2) view of SAC

Table 1. Experimental set components

Part	Materials and Components
SAC case	4 mm aluminum thickness, 1400x800x150 mm
Transparent Cover	12mm thick tempered glass
Absorber Plate	0.5 mm aluminum thickness, 1400x800 mm
Insulation Material	3,5 kg rock wool, thickness 4 cm
Circulation Fan	Stainless steel, (0.15 m³/h, 0.18 kW, 220 V, 50 Hz, 2800 rpm)

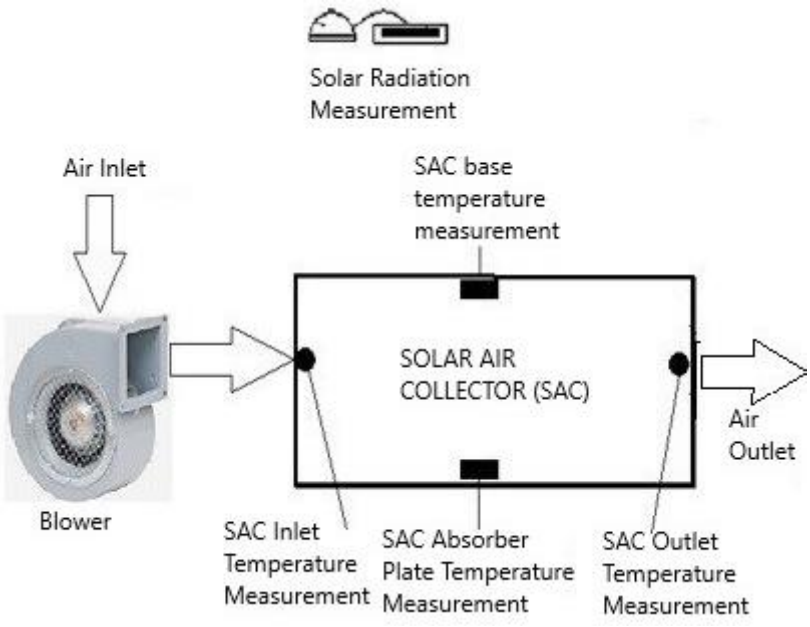

Figure 2. Schematic representation of collector measuring points

Uncertainty Analysis

It has been estimated that both fixed errors, manufacturing errors and random errors are effective for the uncertainties that will arise during the measurement of temperature, air velocity and solar radiation in the SAC. When measuring the value of a parameter, fixed errors, random errors, and errors due to manufacturing errors need to be considered. Equation 1 was used to calculate the total errors resulting from these measured values [14].

$$W_x = [(X_1)^2 + (X_2)^2 + \cdots \ldots \ldots (X_n)^2]^{1/2} \quad (1)$$

Theoretical Calculations

SAC transforms solar energy into usable energy, increasing the heat energy of the fluid passing through it. The SACs work similarly to the working principle of heat exchangers. Solar radiation is transformed into useful fluid heat (Qu) through the SAC absorber plate. Qu is calculated with the help of the following equations [15,16].

$$\dot{Q}_u = \dot{m}_a C_{pa}(T_o - T_i) \quad (2)$$

The useful heat gained by the solar collector is the same as the heat transferred to the working fluid by convection [17]. In this case, Equation 2 can also be expressed by Equation 3.

$$\dot{Q}_u = hA_c(T_{yp} - T_{ort}) \quad (3)$$

The heat transfer coefficients for SACs are calculated as follows [15].

$$h = \frac{\dot{Q}_u}{A_c(T_{yp} - T_{abs})} \quad (4)$$

In Equation 4, T_{yp} is the surface temperature of the absorber plate. The T_{abs} is the average temperature of the air used as a fluid and is obtained by averaging the inlet and outlet temperatures of the collector. All the thermophysical properties of the air are taken according to the mean temperature [18].

$$T_{abs} = \frac{(T_i + T_o)}{2} \quad (5)$$

Table 2 shows the uncertainty values that occur during the measurements of SAC. These values are calculated according to Equation 1.

Table 2. Measurement uncertainties in the experimental set

Measurement parameters	Uncertainty Value
T_{yp} (°C)	±0.50
T_i (°C)	±0.43
T_o (°C)	±0.33
SAC case base temperature T_{ta} (°C)	±0.30
Solar Radiation I (W/m²)	±0.41

Simple linear regression model

Models the relationship between two variables in a simple linear regression (SLR) model. This modeling result can produce a simple linear equation as in Equation 6 based on a single variable [19].

$$Y = \alpha_0 + \alpha_1 X + \varepsilon \quad (6)$$

In Equation 6; Y=Response Variable (Dependent Variable), X=Predictive Variable (Independent Variable), ε =Random Variable (Error Term).

The linearity that appears in Equation 6 is just an assumption. Some further assumptions can be added, such as the independence distribution of Y. The predicted model can predict the Y value based on a given X value.

Multiple linear regression model

In multiple linear regression (MLR), the dependent variable Y is sometimes affected by more than one independent variable. A linear model that relates Y to several estimators can be expressed by Equation 7 [20].

$$Y = \alpha_0 + \alpha_1 X_1 + \alpha_2 X_2 + ... + \alpha_i X_i + \varepsilon \quad (7)$$

Arbitrary constants (α) are called regression coefficients. The error term α provides random variation in Y that predictors cannot explain. Here, multiple variables (X_1, X_2,…X_i) can be used to estimate the Y value.
The data set used in the regression algorithms for the SAC heat transfer coefficient (h) values are shown in Table 3. The maximum and minimum values of the parameters resulting from the experimental measurements are given in the table.

Table3. Input and output parameters for regression models

Input Parameters			
Parameter	**Unit**	**Min.**	**Max.**
T_i	°C	26.8	35.15
T_o	°C	29.3	56.3
T_{yp}	°C	55.2	75.7
T_{ta}	°C	23.2	45.1
I	W/m^2	404.8	926.8
Output Parameter			
Parameter	**Unit**	**Min.**	**Max.**
SAC heat transfer coefficient (h)	W/m^2°C	1.2	18.1

In this study, predictive model equations were created using h values MLR and SLR regression methods. MATLAB2018b software was used to create the predictive model. A total of 252 data were used for each regression. The 210 of these data were used for input values and 42 for output values. Mean absolute percentage error (MAPE), root mean square error (RMSE) analyzes were performed to determine the accuracy between the h values obtained by regression algorithms and the experimental h values. The equations of the MAPE and RMSE analyzes are given below.

$$MAPE = \left(\left| \frac{h_{exp} - T_{predicted}}{T_{exp}} \right| \right) \cdot 100 \quad (8)$$

$$RMSE = \sqrt{\frac{\left(P_h - A_h\right)^2 + ... + \left(P_h - A_h\right)^2}{n}} \quad (9)$$

3. Results

For the SAC heat transfer coefficient calculation, the experimental data made on 1-2 June 2018 were used. The variation of radiation values and SAC absorber plate temperature values measured in the experiments over time are given in Figure 3. According to Figure 3, both radiation and T_{yp} values reached the highest level in the 11:30-13:30.

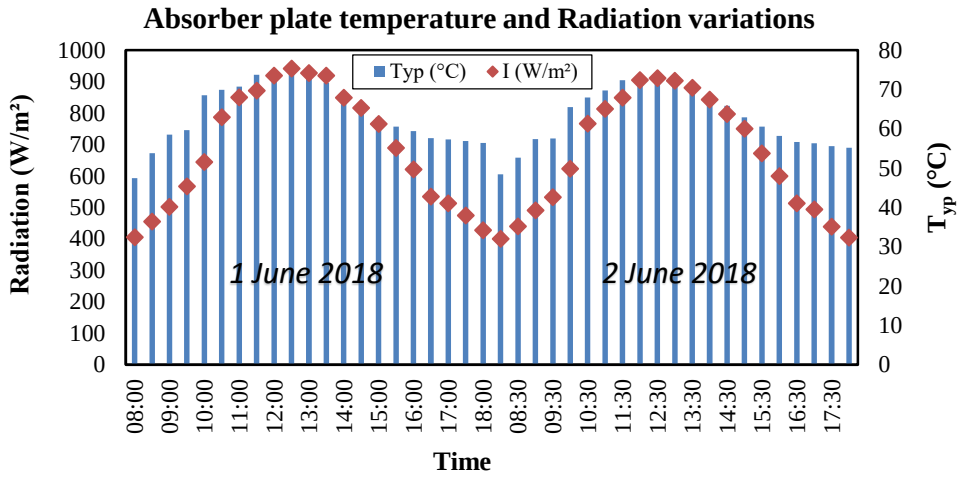

Figure 3. Change of SAC radiation and T_{yp} temperature values

Figure 4 shows the SAC inlet and outlet temperature difference during the experiment. According to Figure 4, where the change in the heat transfer coefficient of the SAC can also be examined, the highest temperature difference and the heat transfer coefficient value at 12:30 are shown as 16.7 °C and 23.4 W/m2 °C, respectively.

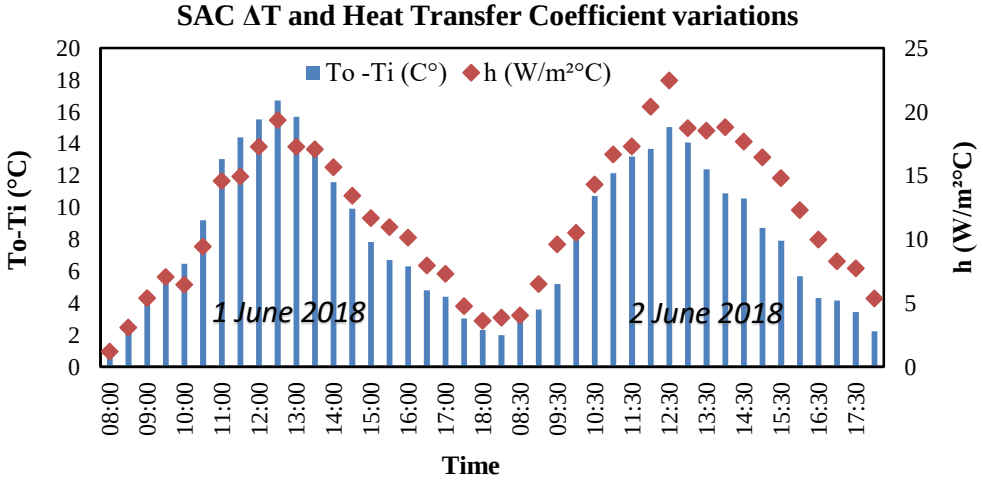

Figure 4. SAC input and output temperature difference and change of h values

Table 4 shows the h equations obtained by regression algorithms and the error analysis results of these equations. The h equation obtained with MLR has less error value than the h equation obtained with SLR.

Table 4. SAC h equations and MAE error values obtained by regression algorithms

MLR h Equation	**MAPE**	**RMSE**
$h\ (W/m^2°C) = 0.7158 * T_i - 0.6571 * T_o + 0.2796 * T_{ta} - 0.3116 * T_{yp} + 0.0051 * I - 1.0629$	0.56	0.073
SLR h Equation	**MAPE**	**RMSE**
$h\ (W/m^2°C) = 0.6 * T_i - 180.75$	0.94	0.011

In studies related to SAC thermal efficiency value MLR modeling in the literature, Vafavei and Sah modeled the SAC efficiency value with an R2 value of 0.947 using MLR [10]. Caner et al. modeled the SAC efficiency value with an RMSE value of 1.2 [12] and Ghritlahre modeled the SAC efficiency value with an R2 value of 0.997 [13]. In this study, the error values of the SAC efficiency value models created with MLR are similar to the studies in the literature.

In Figures 5 and 6, the h values are compared as a result of the equations produced by the regression algorithms, and the experimental h values are given. As shown in Figure 5, the MLR h values are closer to the experimental h values.

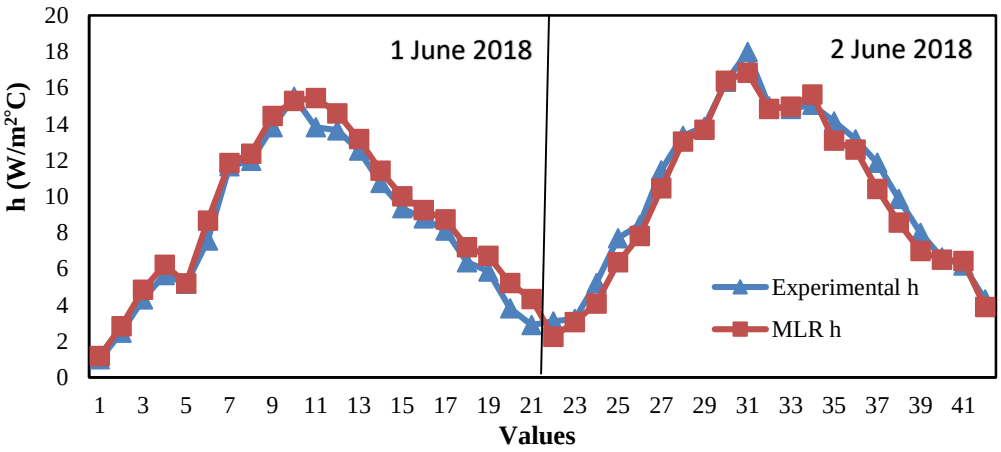

Figure 5. Comparison of SAC experimental h values and MLR h values

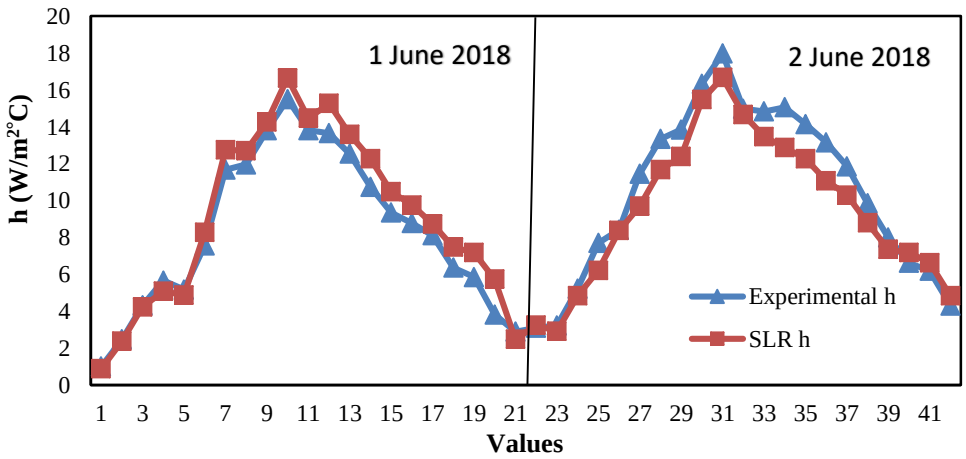

Figure 6. Comparison of SAC experimental h values and SLR h values

Figure 7 shows the convergence between the h values obtained by both regression algorithms and the experimental h values. According to Figure 7, the regression algorithm closest to the experimental values is MLR regression.

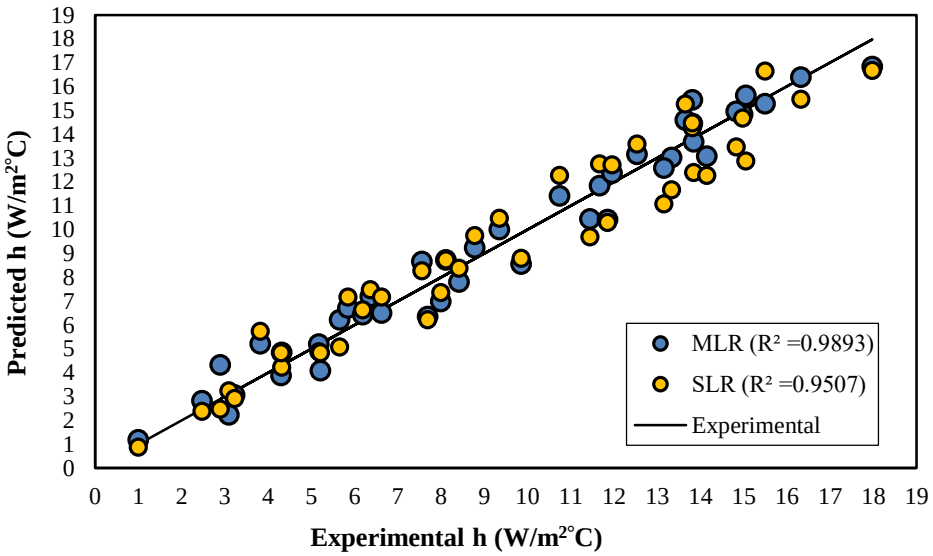

Figure 7. SAC experimental h values and regression h values convergence

4. Conclusions

In this study, the heat transfer coefficient values of an SAC were modeled by multiple and simple regression methods. The resulting model error result has an average absolute error value of 0.6. The values determined by the mathematical h equation obtained by CLR are pretty close to the experimental h values. Equations with fewer error values can be obtained by using more data sets and different machine learning algorithms for the obtained model. It is hoped that the heat transfer coefficient equation obtained as a result of the study can be used in different types of collectors and different experimental conditions.

5. Acknowledgments

This study was supported by Firat University Scientific Research Foundation (Project Numbers MF.17.11 and MF 16.54).

6. Author Contribution Statement

In the study, Author 1 contributed to forming the idea, the analysis of the results, provision of the materials and examination of the results; Author 2 contributed making the design and literature review.

7. Ethics Committee Approval and Conflict of Interest

There is no need for an ethics committee approval in the prepared article. There is no conflict of interest with any person/institution in the prepared article.

Nomenclature

A_c *SAC surface* area (m^2)
Avg Average
T_{yp} SAC absorber plate temperature (°C)

C_{pa} *Air* specific heat at constant pressure (kJ/kgK)
h Heat transfer coefficient (W/ m^2 °C)
I Solar radiation on the collector (W/m^2)
$\dot{m}_a$ *Air m*ass flow rate (kg/s)
Q_u Useful heat of air (W)
SAC Solar air collector
T Temperature (°C)

8. References

[1] Huang MY, Wang MLi, Keovisar V, Li X, Kong D, Yu Q. "Comparative study on energy and exergy properties of solar photovoltaic/thermal air collector based on amorphous silicon cells". *Applied Thermal Engineering*, 185, 116376, 2021.
[2] Arslan E, Aktaş M. "4E analysis of infrared-convective dryer powered solar photovoltaic thermal collector". *Solar Energy*, 208, 46–57, 2020.
[3] Tagnamas Z, Lamsyehe H, Moussaoui H, Bahammou Y, Kouhila M, Idlimam A, Lamharrar A. "Energy and exergy analyses of carob pulp drying system based on a solar collector". *Renewable Energy*, 163, 495–503, 2021.
[4] Ceylan I, Gürel AE. "Solar-assisted fluidized bed dryer integrated with a heat pump for mint leaves". *Applied Thermal Engineering*, 106, 899–905, 2016.
[5] Akpinar EK, Koçyiĝit F. "Energy and exergy analysis of a new flat-plate solar air heater having different obstacles on absorber plates". *Applied Energy*, 87, 3438–3450, 2010.
[6] Tuncer AD, Khanlari A, Sözen A, Gürbüz EY, Şirin C, Gungor A. "Energy-exergy and enviro-economic survey of solar air heaters with various air channel modifications". *Renewable Energy*, 160, 67–85, 2020.
[7] Komolafe CA, Oluwaleye IO, Awogbemi O, Osueke CO. "Experimental investigation and thermal analysis of solar air heater having rectangular rib roughness on the absorber plate". *Case Studies in Thermal Engineering*, 14, 100442, 2019.
[8] Sudhakar P, Cheralathan M. "Thermal performance enhancement of solar air collector using a novel V-groove absorber plate with pin-fins for drying agricultural products: an experimental study". *Journal of Thermal Analysis and Calorimetry*, 140, 2397–2408, 2020.
[9] Norouzian R. *The Palgrave Handbook of Applied Linguistics Research Methodology*. 1nd ed. Palgrave Macmillan, London, Springer, 2018.
[10] Vafaei LE, Sah M. "Predicting efficiency of flat-plate solar collector using a fuzzy inference system". *Procedia computer science*, 120, 221-228, 2017.
[11] Çakmak G, Yıldız C. "The prediction of seedy grape drying rate using a neural network method". *Computers and Electronics in Agriculture*, 75(1), 132-138, 2011.
[12] Caner M, Gedik E, Keçebaş A. "Investigation on thermal performance calculation of two type solar air collectors using artificial neural network". *Expert Systems with Applications*, *38*(3), 1668-1674, 2011.
[13] Ghritlahre HK, Prasad RK. Investigation of thermal performance of unidirectional flow porous bed solar air heater using MLP, GRNN, and RBF models of ANN technique". *Thermal Science and Engineering Progress*, *6*, 226-235, 2018.
[14] Holman JP. *Experimental methods for engineers*. Eight Edit, McGraw-Hill, New York, 2012.
[15] Acır A, Ata İ. "A study of heat transfer enhancement in a new solar air heater having circular type turbulators". *Journal of the Energy Institute*, 89, 606–616, 2016.
[16] Devecioglu AG, Oruc V. "Experimental investigation of thermal performance of a new solar air collector with porous surface". *Energy Procedia*. 113, 251–258, 2017.
[17] Acir A, Ata I, Canli ME. "Investigation of effect of the circular ring turbulators on heat transfer augmentation and fluid flow characteristic of solar air heater". *Experimental Thermal and Fluid Science*, 77, 45–54, 2016. https://doi.org/10.1016/j.expthermflusci.2016.04.012.
[18] Acır A, Canlı ME, Ata İ, Çakıroğlu R. "Parametric optimization of energy and exergy analyses of a novel solar air heater with grey relational analysis". *Applied Thermal Engineering*, 122, 330–338, 2017.
[19] Sreehari E, Pradeep Ghantasala GS. "Climate changes prediction using simple linear regression". *Journal of Computational and Theoretical Nanoscience*, 16, 655–658, 2019.

[20] Mahaboob B, Praveen JP, Appa Rao BV, Harnath Y, Narayana C, Prakash GB. "A study on multiple linear regression using matrix calculus". *Advances in Mathematics: Scientific Journal*, 9, 4863–4872, 2020.

Firat Univ Jour. of Exp. and Comp. Eng., 1(1), 24-30, 2022

Firat University Journal of Experimental and Computational Engineering
Fırat Üniversitesi Deneysel ve Hesaplamalı Mühendislik Dergisi

Obtaining and modeling the relaxation modulus of self-healing asphalt mixtures

Kendini iyileştiren asfalt karışımlarının rölaksasyon modüllerinin elde edilmesi ve modellenmesi

Bahadır YILMAZ[1], Ahmet Münir ÖZDEMİR [2*]

[1,2]Civil Engineering, Engineering and Natural Sciences, Bursa Technical University, Bursa, Turkey.
[1]bahadir.yilmaz@btu.edu.tr, [2]ahmet.ozdemir@btu.edu.tr

Received: 20.10.2021
Accepted: 10.01.2022
Revision: 28.12.2021
doi: 10.5505/fujece.2022.43531
Research Article

Abstract
In this study, pure and self-healing asphalt mixture samples were obtained by adding capsules containing waste vegetable oil to mixtures at 0.25, 0.50, 0.75 and 1.00% ratios. Afterwards, creep test with a constant stress was carried out on the samples, and the resistance of asphalt mixtures against permanent deformation was investigated. Relaxation modulus values were obtained by using the creep compliance values that measured at the end of the experiment with mathematical transformations. Then, the relaxation modulus results were fitted to the Generalized Maxwell Model, which is a common model used to represent the viscoelastic properties of asphalt mixtures, and Prony series parameters were obtained. The results showed that the addition of capsule reduced the permanent deformation strength of the asphalt mixture. In addition, the curve fitting processes were successfully performed and the desired parameters were obtained with high accuracy.

Keywords: Asphalt, Microcapsule, Waste vegetable oil, Relaxation modulus, Generalized Maxwell Model

Özet
Bu çalışmada atık bitkisel yağ içeren kapsüller 0.25, 0.50, 0.75 ve 1.00% oranlarında asphalt karışımlara ilave edilerek, saf ve kapsüllü olmak üzere numuneler elde edilmiştir. Daha sonra elde edilen numuneler üzerinde sabit bir gerilme değerinde sünme deneyi gerçekleştirilerek, kapsül ilavesinin asfalt karışımların kalıcı deformasyona karşı dayanımları incelenmiştir. Deney sonucu ölçülen sünme uyumu değerlerinden, matematiksel dönüşümlerden faydalanılarak gevşeme modülü değerleri elde edilmiştir. Daha sonra gevşeme modülü sonuçları, asfalt karışımların viskoelastik özelliklerini temsil etmek için kullanılan yaygın bir model olan Genelleştirilmiş Maxwell Modeli'ne eğri uydurma yöntemi ile uydurularak Prony serisi parametreleri elde edilmiştir. Sonuçlar, kapsül ilavesinin asfalt karışımının kalıcı deformasyon dayanımını düşürdüğünü göstermiştir. Ayrıca eğri uydurma işlemleri başarıyla gerçekleştirilerek yüksek doğrulukta istenilen parametreler elde edilmiştir.

Anahtar kelimeler: Asfalt, Mikrokapsül, Atık bitkisel yağ, Gevşeme modülü, Genelleştirilmiş Maxwell Modeli

1. Introduction

In asphalt mixtures, bitumen undertakes the task of binding the materials in the mixture, and aggregates undertake the task of forming the skeleton structure [1]. After the mixture is laid and compacted, the top course of the pavement becomes the wearing course. For this reason, loads and environmental effects can cause significant damage to this course during its service life [2]. Pavement engineers and researchers have done a wide variety of studies to improve the properties of the wearing course [3–8]. The most common application is to modify the bitumen. In this way, resistance against environmental effects and axle loads is strengthened and a bitumen with desired properties is obtained [9–13].

There has been a lot of talk lately about self-healing materials. As a wide variety of building materials are included in the self-healing concept, asphalt mixtures have also been included in this method and many studies have been carried out [14–16]. In their study, Garcia-Hernandez and his team aimed to improve the reflection cracks by adding microcapsules to the asphalt mixture [17]. Gomez-Meijide and his team added metal particles to the mixture in order to improve the asphalt

*Corresponding author

mixture by induction heating method and obtained successful results [18]. Yamaç et al. added capsules containing waste vegetable oil to the mastic asphalt mixture and concluded that the encapsulated samples showed 80% higher recovery than the pure samples [15]. Yalçın achieved improvement by adding waste metals to the asphalt mixture and then subjecting it to microwave heating. It was determined that the self-healing ability increased, but the mechanical properties of the asphalt mixture were negatively affected [19].

In this study, capsules containing waste vegetable oil were added to the asphalt mixture and the creep test was carried out. Then, relaxation modulus values were obtained from the creep compliance values by using mathematical transformation methods. In this way, relaxation property, which is an important concept in determining viscoelastic properties, could also be examined. Then, relaxation modulus values were fitted to the Generalized Maxwell Model, which is a common viscoelastic model known to successfully reflect the properties of viscoelastic materials, and various evaluations were made.

2. Materials and Method

Within the scope of the study, it is aimed to create cracks in the mixture, and to repair the cracks by releasing the waste oils in the capsules added to the mixture by breaking the capsules. For this reason, B 50/70 bitumen, which is a pavement grade bitumen with a high consistency, was obtained from TÜPRAŞ Batman refinery in order to determine the improvement more clearly. In the study, limestone (limestone) type crushed stone material obtained from Elazig Karayazı Region was used as aggregate. In the mixture design, the Superpave design method was adhered to. The gradation was given in Table 1 and Figure 1.

Table 1. Aggregate gradation

Sieve size (mm)	Percent passing (%)	Control values		Restricted Area	
		Min.	**Max.**	**Min.**	**Max.**
19 (3/4”)	100	100			
12.5 (1/2”)	95	90	100		
9.5 (3/8”)	88		90		
4.75 (No. 4)	65				
2.36 (No. 8)	35	28	58	39.1	39.1
1.18 (No. 16)	23			25.6	31.6
0.6 (No. 30	14			19.1	23.1
0.3 (No. 50)	10			15.5	15.5
0.15 (No. 100)	8				
0.075 (No. 200)	5	2	10		

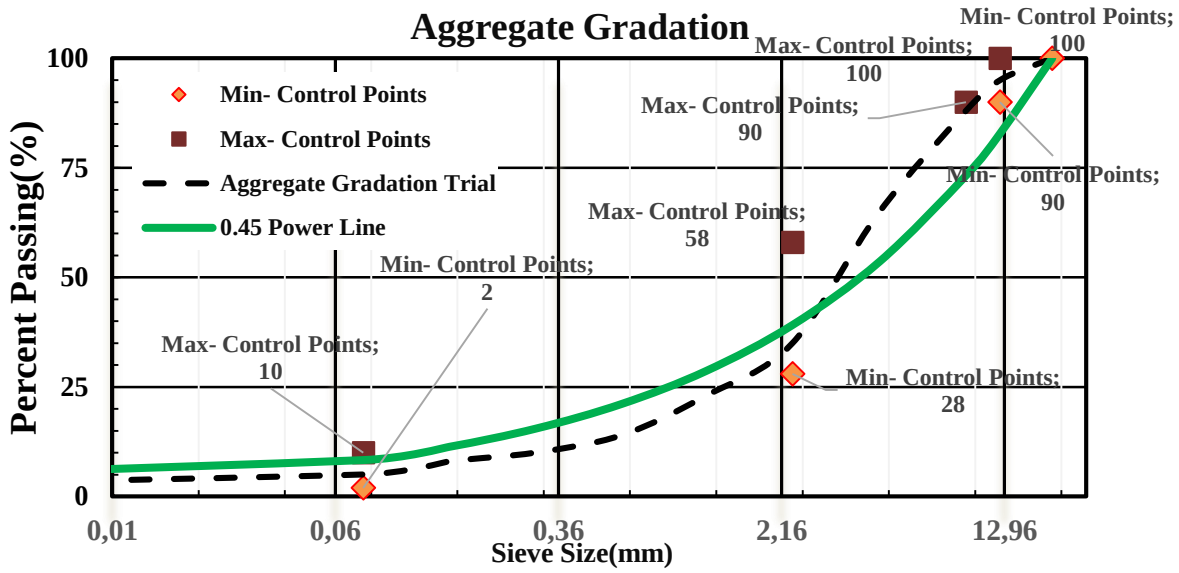

Figure 1. Aggregate gradation

By following the steps and materials in the previous studies in capsule production, capsules containing waste vegetable oil were obtained [15]. The produced capsules were added to the asphalt mixture at the rates of 0.25%, 0.50%, 0.75% and 1.00%, and encapsulated mixtures were obtained. The optimum bitumen content was determined as 4.67%.

2.1. Creep test

Creep test was carried out to investigate the permanent deformation behavior of pure and encapsulated asphalt mixtures under cyclic loads. Permanent deformation under cyclic loads often results in rutting problem. In the dynamic creep test, a constant load is applied to the surface of the cylindrical sample repeatedly for a certain period of time. With the help of LVDTs adjusted vertically on the metal plate placed on the surface of the sample, plastic and elastic deformations that occur at each load repetition can be detected. The experimental setup inside the air-conditioning cabinet is shown in Figure 2. As a result of the experiment, deformation values are obtained depending on the number of load repetitions. In this experiment, the period is approximately 1 second, so the number of load repetitions can also be considered as the total time. In the study, the experiment was carried out by applying a constant load of 450 kPa at 40°C.

Figure 2. Dynamic creep test

When the time-dependent strain values obtained as a result of the creep test performed under a constant stress ($\sigma 0$), $\varepsilon(t)$ are divided by the applied constant stress, time-dependent creep compliance values ($J(t)$) will be obtained (Equation 1) [20].

$$J(t) = \frac{\varepsilon(t)}{\sigma_0} \quad (1)$$

where J(t) is the creep compliance at any time t (1/MPa), ε(t) is the strain at any time t, and σ_0 is the constant stress (MPa).

Then, the creep compliance values obtained were converted to relaxation modulus as in the study of Kim et al. In the aforementioned study, the process was carried out according to the solution proposed by Christiansen [21].

3. Results

3.1. Creep compliance results of asphalt mixtures

The creep compliance curves of pure and capsule added asphalt mixtures are given in Figure 3.

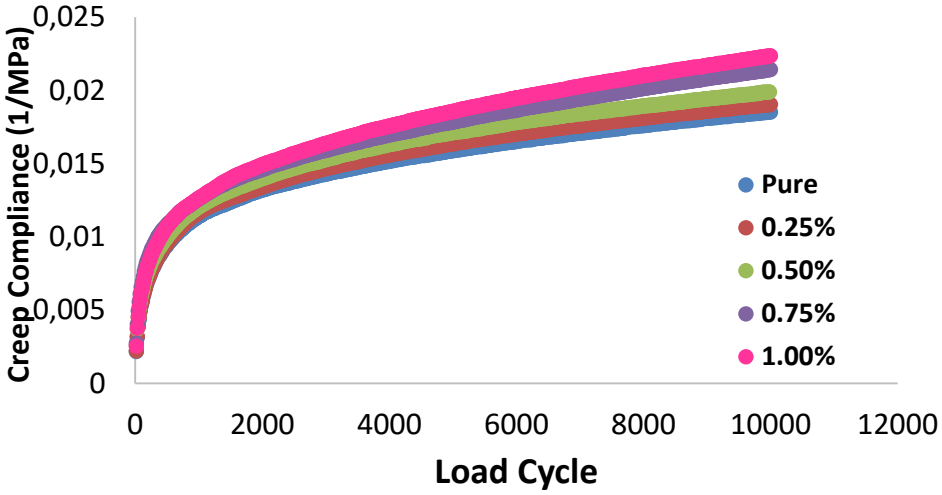

Figure 3. Creep compliance curves of pure and capsule added mixtures

When Figure 3 is examined, a rapid increase was observed in the creep compliance curves in all samples at the beginning, then this curve grows slowly and becomes almost linear. While the mixture with 1.0% capsule added had the highest creep compliance value, the lowest creep compliance value was obtained in the pure mixture. The reason for this is that as the loading time (number of load repetitions) increases, it releases the oil in the capsule and softens the mixture. Therefore, with the decrease of the creep stiffness, in other words, the creep strength, the creep compliance value increases. Final Creep compliance values increased by 2.81, 7.48, 15.61 and 20.77% for capsule contents (0.25, 0.50, 0.75, 1.00%) compared to pure mixture, respectively.

3.2. Relaxation modulus results of asphalt mixtures

As mentioned in the method part of the asphalt mixture samples, the relaxation modulus values obtained from the creep compliance results are given in Figure 4.

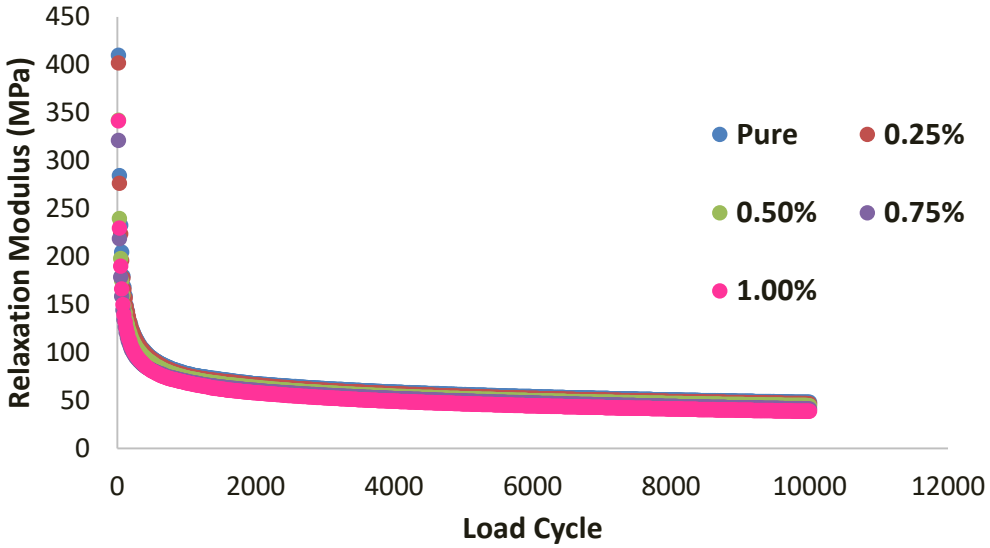

Figure 4. Relaxation modulus curves obtained by the interconversion method

The weakening process of the relaxation modulus, which is an important parameter in defining the viscoelastic behavior, is examined in three stages. In the first stage, the relaxation modulus falls rapidly in a short time and the maximum decrease occurs in this stage. In the second stage, the return of this drop takes place, the rate of fall now slows down and the range it drops is 30% of the initial stiffness modulus. In the third stage, the relaxation modulus values of the mixture became stable. The amount of decrease at this stage is small. According to Figure 4, it is seen that relaxation modulus values decrease rapidly in all samples. The reason for this is the gradual dissipation of the internal stress in the asphalt mixture. In a subtitle, relaxation modulus values will be fitted to the generalized Maxwell model and these features will be interpreted in more detail. In addition, it is seen that the relaxation modulus values of asphalt mixtures decrease with the increase of the capsule ratio. The final relaxation modulus values were increased by 3.15, 7.34, 14.36 and 19.56% for the capsule contents (0.25, 0.50, 0.75, 1.00%) compared to the pure mixture.

3.3. Analysis of relaxation behavior of based on Generalized Maxwell Model

Generalized Maxwell Model was chosen to examine the viscoelastic behavior of asphalt mixture samples in relaxation state. It is known that this model strongly agrees with the relaxation modulus values of viscoelastic materials and successfully represents this behavior. The Generalized Maxwell model equation is given in Equation 2 and the schematic representation of the model is given in Figure 5.

$$E(t) = E_\infty + \sum_{i=1}^{n} E_i e^{-t/\rho_i} \quad (2)$$

where E(t) is the relaxation modulus, E_∞ is the equilibrium relaxation modulus, t is the time, ρ_i is the relaxation n time.

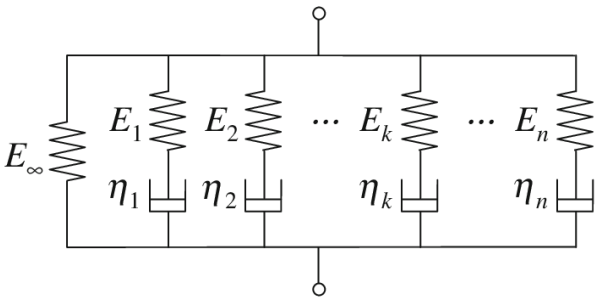

Figure 5. Generalized Maxwell Model [22]

Prony series fitting parameters of the relaxation modulus of the asphalt mixture was given in Table 2.

Table 2. Prony series results of relaxation modulus

	0%	0.25%	0.50%	0.75%	1.00%
E∞	3.99E+01	2.61E+01	2.96E+01	2.52E+01	3.31E+01
E1	2.36E+01	5.62E+01	3.19E+02	7.62E+01	2.85E+01
E2	9.30E+01	4.48E+02	5.96E+01	3.27E+01	3.11E+01
E3	3.09E+01	3.16E+01	2.01E+02	3.13E+01	6.18E+01
E4	6.39E+01	7.12E+01	2.67E+01	2.82E+02	3.19E+01
E5	2.03E+02	3.35E+01	3.95E+01	1.02E+02	3.11E+01
E6	3.84E+01	2.68E+01	6.40E+01	1.65E+01	1.98E+02
E7	6.94E+02	4.18E+01	2.84E+01	1.06E+02	8.21E+01
R^2	0.999	0.999	0.999	0.999	0.999

When Table 2 is examined, it is seen that the R^2 values in each capsule content are above 0.99 and the fitting process is performed with high accuracy. Because of the Generalized Maxwell Model has too many parameters, it is difficult to obtain a regular variation. For this reason, some fluctuations occurred in the values. However, it has been observed that this model successfully describes the viscoelastic properties of asphalt mixtures, with the successful fitting of the model with high accuracy. In addition, it can be thought that these fluctuations occur because the relaxation modulus values are realized by a mathematical transformation rather than an experimental one.

4. Discussion

In this study, pure and self-healing samples were obtained by adding capsules containing waste vegetable oil to asphalt mixtures at 0.25, 0.50, 0.75 and 1.00% ratios. Afterwards, a constant stress value creep test was carried out on the samples obtained, and the resistance of the capsule addition of asphalt mixtures against permanent deformation was investigated. The results obtained are summarized below:

- With the addition of capsule, the permanent deformation strength of the mixture decreased. As the capsule ratio increases, the decrease is greater compared to the pure mixture.
- According to the creep compliance data, it can be said that the rejuvenator in the capsules breaks with the loading and softens the mixture.
-According to the relaxation modulus results, it is seen that the values decrease with the dissipation of the internal stress in the mixture. The mixture containing 1.00% capsule has the lowest final relaxation modulus.
-Relaxation modulus results were evaluated with the Generalized Maxwell Model. The results showed that relaxation modulus values can be modeled and explained with this model with very high accuracy and low error.

5. Author Contribution Statement

In the study, Author 1 contributed to forming the idea, the analysis of the results, provision of the materials and examination of the results; Author 2 contributed making the design, checking the article in terms of content and literature review.

6. Ethics Committee Approval and Conflict of Interest

There is no need for an ethics committee approval in the prepared article. There is no conflict of interest with any person/institution in the prepared article.

7. References

[1] Hunter R, Self A, Read J. *The Shell Bitumen Handbook*, 6th edition. London, England, Shell Bitumen, 2015.
[2] Hu M, Li L, Peng F. "Laboratory investigation of OGFC-5 porous asphalt ultra-thin wearing course". *Construction and Building Materials*, 219, 101–110, 2019.
[3] Jia H, Chen H, Sheng Y, Meng J, Cui S, Kim YR, *et al.* "Effect of laboratory aging on the stiffness and fatigue cracking of asphalt mixture containing bamboo fiber". *Journal of Cleaner Production*, 333, 130120, 2021.
[4] Fu L, Jiao Y, Chen X. "Reinforcement evaluation of different fibers on fracture resistance of asphalt mixture based on acoustic emission technique". *Construction and Building Materials*, 314, 125606, 2022.
[5] Sun S, Li P, Cheng L, Wang X, Zhang W. "Analysis of skeleton contact stability of graded aggregates system and its effect on slip creep properties of asphalt mixture". *Construction and Building Materials*, 316, 125911, 2022.
[6] Zhao X, Sheng Y, Lv H, Jia H, Liu Q, Ji X, *et al.* "Laboratory investigation on road performances of asphalt mixtures using steel slag and granite as aggregate". *Construction and Building Materials*, 125655, 2021.
[7] Karami M, Nikraz H. "Using advanced materials of granular bra modifier binder to ımprove the flexural fatigue performance of asphalt mixtures". *Procedia Engineering*, 125, 452–460, 2015.
[8] Wulandari PS, Tjandra D. "Use of crumb rubber as an additive in asphalt concrete mixture". *Procedia Engineering*, 171, 1384–1389, 2017.
[9] Apostolidis P, Liu X, Erkens S, Scarpas A. "Evaluation of epoxy modification in bitumen". *Construction and Building Materials*, 208, 361–368, 2019.
[10] Muhammed Ertugrul Ç, Mehmet Y, Kök BV, Yalçin E. "Effects of various biochars on the high temperature performance of bituminous binder". *In Proceedings of 6th Eurasphalt & Eurobitume Congress*. Czech Technical University in Prague, 1-3 June 2016.
[11] Erkuş Y, Kök BV, Yilmaz M. "Effects of graphite on rheological and conventional properties of bituminous binders". *International Journal of Pavement Research and Technology*, 10(4), 315–321, 2017.
[12] Erkuş Y, Kök BV, Yilmaz M. "Evaluation of performance and productivity of bitumen modified by three different additives". *Construction and Building Materials*, 261, 120553, 2020.
[13] Vural Kök B, Aydoğmuş E, Yilmaz M, Akpolat M. "Investigation on the properties of new palm-oil-based polyurethane modified bitumen". *Construction and Building Materials*, 289, 123152, 2021.
[14] Sun D, Sun G, Zhu X, Guarin A, Li B, Dai Z, *et al.* "A comprehensive review on self-healing of asphalt materials: Mechanism, model, characterization and enhancement". *Advances in Colloid and Interface Science*, 256, 65-93, 2018.
[15] Yamaç ÖE, Yilmaz M, Yalçın E, Kök BV, Norambuena-Contreras J, Garcia A. "Self-healing of asphalt mastic using capsules containing waste oils". *Construction and Building Materials*, 270, 121417, 2021.
[16] Norambuena-Contreras J, Liu Q, Zhang L, Wu S, Yalcin E, Garcia A. "Influence of encapsulated sunflower oil on the mechanical and self-healing properties of dense-graded asphalt mixtures". *Materials and Structures*, 52(4), 78, 2019.
[17] Garcia-Hernández A, Salih S, Ruiz-Riancho I, Norambuena-Contreras J, Hudson-Griffiths R, Gomez-Meijide B. "Self-healing of reflective cracks in asphalt mixtures by the action of encapsulated agents". *Construction and Building Materials*, 252, 118929, 2020.
[18] Gómez-Meijide B, Ajam H, Lastra-González P, Garcia A. "Effect of air voids content on asphalt self-healing via induction and infrared heating". *Construction and Building Materials*, 126, 957–966, 2016.
[19] Yalcin E. "Effects of microwave and induction heating on the mechanical and self-healing characteristics of the asphalt mixtures containing waste metal". *Construction and Building Materials*, 286, 122965, 2021.
[20] Kim YR. *Modeling of Asphalt Concrete*. Ed: Kim YR New York: McGraw-Hill Education, 2009.
[21] Park SW, Kim YR. "Interconversion between Relaxation Modulus and Creep Compliance for Viscoelastic Solids". *Journal of Materials in Civil Engineering*, 11(1), 76–82, 1999.
[22] Chae S-H, Zhao J-H, Edwards DR, Ho PS. "Characterization of the Viscoelasticity of Molding Compounds in the Time Domain". *Journal of Electronic Materials*, 39(4), 419–425, 2010.

Firat Univ Jour. of Exp. and Comp. Eng., 1(1), 31-42, 2022

Firat University Journal of Experimental and Computational Engineering
Fırat Üniversitesi Deneysel ve Hesaplamalı Mühendislik Dergisi

Using computational fluid dynamics for wave generation and evaluation of results in numerical wave tank modelling

Sayısal dalga tankı benzetiminde dalga üretimi ve sonuçların değerlendirilmesi amacıyla hesaplamalı akışkanlar dinamiği kullanılması

Halil İbrahim YAMAÇ[1*], Ahmet KOCA[2], Taner YILMAZ[3]

[1,2,3]Department of Mechatronics Engineering, Fırat University, Elazığ, Turkey.
[1]halilymc@gmail.com, [2]a.koca@firat.edu.tr, [3]t.yilmaz@firat.edu.tr

Received: 30.12.2021
Accepted: 31.01.2022
Revision: 20.01.2022
doi: 10.5505/fujece.2022.76486
Case Report

Abstract
In this paper, computational modeling of wave generation and evaluation of results are given. The analysis of Computational Fluid Dynamics is performed in the ANSYS Fluent module. The model of numerical analysis is made time-dependent. The Numerical Wave Tank is an engineering research equipment for studying sea waves that requires the least amount of people and materials. The Numerical Wave Tank may be used to simulate the motion of the ocean and sea waves with a modeled moving wall as a wave-maker. To generate regular gravity waves, a Numerical Wave Tank based on Reynolds Averaged Navier Stokes equations and the Volume of Fluid technique is modeled using Dynamic Mesh Technique. Wave heights, water depths, wavelength and wave periods are chosen variable parameters. Water volume fraction, velocities, turbulence kinetic energy and dynamic pressure are evaluated results. A brief explanation of how to generate waves influence is made.

Keywords: Computational fluid dynamics, Volume of fluid method, Numerical wave tank, Dynamic mesh technique, User defined function

Özet
Bu makalede, dalga üretiminin hesaplamalı modellemesi ve sonuçların değerlendirilmesi verilmektedir. Hesaplamalı Akışkanlar Dinamiğinin analizi ANSYS Fluent modülünde gerçekleştirilir. Sayısal analiz modeli zamana bağlı yapılmıştır. Sayısal Dalga Tankı, deniz dalgası konusunda en az insan gücü ve malzeme kaynağı gerektiren mühendislik araştırma aracı olarak düşünülebilir. Sayısal Dalga Tankı, dalga yapıcı olarak hareketli duvar modelleme ile okyanus ve deniz dalgalarının hareketini simüle etmek için kullanılabilir. Reynolds-Ortalamalı Navier-Stokes denklemlerine ve Akışkan Hacmi yöntemine dayalı Sayısal Dalga Tankı, düzenli yerçekimi dalgaları oluşturmak için Dinamik Ağ Tekniği kullanılarak modellenmiştir. Dalga yükseklikleri, su derinlikleri, dalga boyu ve dalga periyotları değişken parametreler olarak seçilmiştir. Su hacim oranı, hızlar, türbülans kinetik enerjisi ve dinamik basınç sonuçları değerlendirilmiştir.

Anahtar kelimeler: Hesaplamalı akışkanlar dinamiği, Akışkan hacmi yöntemi, Sayısal dalga tankı, Dinamik ağ tekniği, Kullanıcı tanımlı fonksiyon

1. Introduction

Renewable energy systems are sustainable by means of energy production. It can be said that they have huge potential. It is an undeniable fact that waves are potential energy source. Many studies and designs have been done on energy generating systems in the ocean and sea. These studies are about energy generation, designing breakwaters or floating behavior of ships. There are many studies on Numerical Wave Tanks (NWT). Waves on the sea surface are periodical water movements. Waves have mixed random properties. Large amounts of energy can be transformed into electrical power via wave motions [1]. Fluid behavior due to wave breakers in a non-hydrostatic system and the effect of the fluid on wave breakers can be investigated numerically. Changes in the wave profile can be observed due to wave breaks [2]. In the work done by Finnegan and Goggins, ocean waves are modeled on a NWT to study fluid / solid interactions. The wave energy conversion system has been studied for a floating body. When comparing analytical studies with numerical

*Corresponding author

simulations, water particle movements are evaluated depending on the time. The model has been achieved with better results for high-amplitude and low-frequency waves [3]. Bhinder et al. discover the forces of fluid impact on the production of power in wave energy converting systems with using Computational Fluid Dynamics (CFD) simulations. System efficiency as a function of time is investigated in relation to the forces acting in the fluid environment. Waves having the desired property can be created using simulations. [4]. In the examination of fluid-solid interactions, Hu et al. 2016 use CFD for modeling waves to see how forces behave with structures that have variable shapes [5]. Liaghat discusses the analyses of the force interaction by means of fluid-solid and makes simulations on the fluid-based force effect of the solid structure of materials in his master's thesis. The convergence of waves with a solid body is the result of the momentum water effect on solid movements that are transferred to the surface of the final solids. In order to observe the interaction numerically, it is first necessary to create waves. The NWT simulations are made with different assumptions in CFD programs. Waves with certain qualities can be created using simulations [6]. In a study by Liu et al., a numerical simulation with Reynolds-Averaged-Navier-Stokes (RANS) equation is done for two-dimensional NWT modeling utilizing the Volume of Fluid (VOF) approach[7]. In the study by Wang and Liu, time-dependent wave generation is performed and the time-dependent change of the surface height parameter is obtained [8]. In the study performed by Zhu et al., RANS equations are used in the NWT model. It is also defined that momentum sources can be added to the CFD program using User Defined Functions (UDF) to create different regions. NWT is divided into regions where the waves have optimal modes such as wave generator wave formation and wave damping [9]. In a study by Oijeh et al., A kinematic study of extreme wave models is performed using RANS equations and VOF simulations. The highest (extreme) waves observed on the sea surface are examined [10]. Liang et al. said that extreme waves to be generated in the NWT are modeled. It is found that the variable properties of the generated non-uniform waves are appropriate. The horizontal velocities were obtained from the numerical and experimental results [11]. In this study, a two-dimensional (2D) NWT model is created. UDF is used to simulate waves in the 2D environment. How to generate waves, how the results are obtained from the simulation environment are explained briefly.

2. Materials and Method

The Fluent Module is used to generate waves in this investigation. The gravitational waves that occur on a regular basis are modeled. The waves have a sinusoidal shape, and their behavior does not alter at each time step. When an object is tossed into a tank of water, it causes irregularity and surface waves. The alignment of the water to its initial state as a result of gravity's acceleration causes the movements on the water's surface. Gusts can even be blamed for causing free surface waves. The wavelength equation is shown in Equation 1:

$$L = \frac{gT^2}{2\pi} \tanh\left(\frac{2\pi h}{L}\right) \tag{1}$$

Where the depth of water is h, the length of the wave is L, the acceleration of gravity is g, the period of the wave is T. The time it takes for a wave to form is known as its period. The amount of time it takes for a length of a wave to form. Depending on the linear or nonlinear parameters, wave generation varies according to boundary conditions and physical realities [12]. Free surface dynamic, surface and bottom conditions can be called boundary conditions of gravitational waves.

2.1. Governing Equations

The solver in Fluent uses the finite volume methodology as its foundation. The governing equations are discretized and solved repeatedly across each sub-region using this technique, which separates the region of interest into sub-regions. As a result, the value of each variable's approximation at places in the domain is attained. In the Fluent module, the Pressure Implicit with Splitting of Operator (PISO) Solver is employed. The pressure-velocity connection diagram is part of the SIMPLE algorithm family, which relies on a high degree of approximation of the relationship between pressure and velocity. The limitation of the SIMPLE and SIMPLEC algorithms is that they do not provide the momentum balance of the new velocity and approximate flow values after the pressure verification equation is solved. As a result, the solution should be repeated until equilibrium is achieved. The PISO algorithm uses two extra corrections to increase the effectiveness of this calculation. Adjoining correction and asymmetry correction are two of them. The Navier-Stokes

equations are applied directly to the system by the SIMPLE and SIMPLEC algorithms, with the parameters added after the user selects them [13]. The equations of continuity of mass and Navier Stokes are [14]:

$$\frac{\partial \rho}{\partial t}+\frac{\partial(\rho u)}{\partial x}+\frac{\partial(\rho w)}{\partial z}=0 \tag{2}$$

$$\rho\left(\frac{\partial u}{\partial t}+u\frac{\partial u}{\partial x}+w\frac{\partial u}{\partial z}\right)=-\frac{\partial p}{\partial x}+2\mu\frac{\partial^2 u}{\partial x^2}+\frac{\partial}{\partial z}\left(\mu\left(\frac{\partial u}{\partial z}+\frac{\partial w}{\partial x}\right)\right)+F_x \tag{3}$$

$$\rho\left(\frac{\partial w}{\partial t}+u\frac{\partial w}{dx}+w\frac{\partial w}{\partial z}\right)=-\frac{\partial p}{\partial z}+2\mu\frac{\partial^2 w}{\partial z^2}+\frac{\partial}{\partial x}\left(\mu\left(\frac{\partial u}{\partial z}+\frac{\partial w}{\partial x}\right)\right)-\rho g+F_z \tag{4}$$

for the 2D NWT, the x and y are coordinate system positions, the fluid density of the fluid is ρ, the pressure is p, the velocity in the horizontal direction is u, the velocity in the vertical direction is v, time is t, the viscosity is μ. The dynamic pressure values are calculated from the solver by using formulation V is velocity magnitude, Equation 5 shows the Dynamic pressure [13]:

$$P_d=\frac{\rho_m-\rho_o}{2}V^2 \tag{5}$$

2.2. Numerical wave tank

Fluent was used to simulate 2D NWT. If it is not intended to obtain side effects, the difference between 2D and 3D analysis results can be considered the same. Because the average variables on lines in 2D are the same with the average variables on areas in 3D. When 3D modelling is made, Data are reviewed and plotted on a plane parallel to the wave motion.
In this study, when waves are generated in the NWT, a piston wavemaker is used. The tank's left wall acts as a wave generator. The UDF is used to move the wall on a regular basis. During the investigation, transient analysis is employed. PISO algorithm is used as solver with k-epsilon (k-ε) Turbulence Model, Realizable Wall Functions, Pressure Based VOF model. Dynamic Mesh settings is used. The NWT is shown in Figure 1.

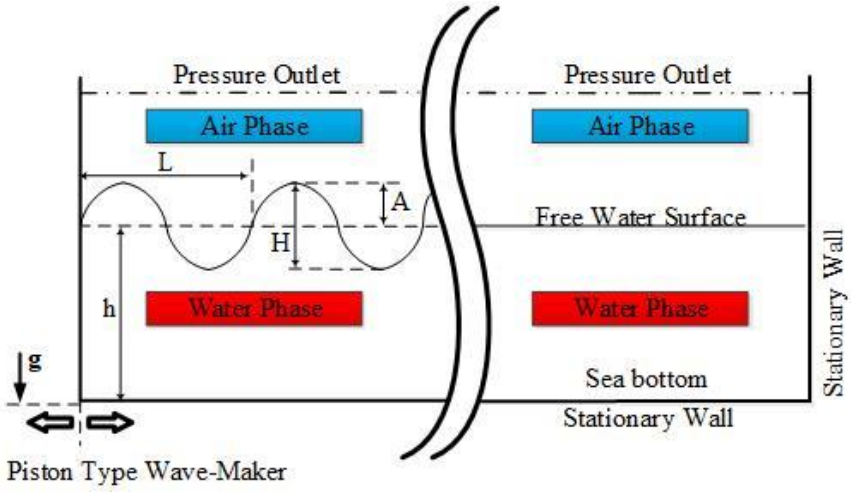

Figure 1. Numerical wave tank

The NWT simulation is done with a tank that is 200 meters long. The differences between the examples in this study are the initial depth of water and wave height. The fluent module employs the VOF approach. This approach is frequently

utilized in the Fluent module's time-dependent solutions. Multiple immiscible fluids are modeled using the VOF approach. The volume fraction parameter is used in the VOF method formulation to model a mixture of two or more phases. There are two phases in the simulation, which are air and water. In Table 1, the qualities of phases are listed.

Table 1. Material properties used in fluent

Name of Material	Density	Viscosity
Air	1.225 kg/m^3	1.7894x10^{-5} kg/ms
Water-liquid	998.2 kg/m^3	0.001003 kg/ms

The volume fraction in the computed cells is defined as a variable for each phase contributed to the model. At each control volume, the volume fractions are combined. For all variables and characteristics, fields by phase and average volume values are shared. For each phase, the volume fraction values of each zone are determined in separate regions. The features and variables in the cells are represented as one of the phases or a mixture in the cells. α_q can be used to represent a volume fraction. There are three scenarios in which α_q [13]:

•if $\alpha_q = 0$, then cell q (q=1,2,3...) is empty for numbering fluids.
•if $\alpha_q = 1$, then cell q (q=1,2,3...) is full for numbering fluids.
•if $0 < \alpha_q < 1$, then cell q (q=1,2,3...) have phases of more than one in the cell.
α_q using regional values, each control volume in the relevant area is given the required variables and attributes.

$$\frac{1}{\rho_q}\left[\frac{\partial}{\partial_t}\left(\rho_q\alpha_q\right)+\nabla\left(\rho_q\alpha_q\vec{v}_q\right)\right]=S_{\alpha_q}+\sum_{p=1}^{n}\left(\dot{m}_{rq}-\dot{m}_{qr}\right) \tag{6}$$

where, the mass transfer (instantaneous) from q phase to r phase is $\dot{m}_{qr}$, the mass transfer (instantaneous) from r phase to q phase is $\dot{m}_{rq}$, for initial conditions S_{α_q} is zero, also with UDF, S_{α_q} is added in Equation 6. The equation of momentum is:

$$\frac{\partial}{\partial t}\left(\rho\vec{v}\right)+\nabla\left(\rho\vec{v}\vec{v}\right)=-\nabla P+\nabla.\left[\mu\left(\nabla\vec{v}+\nabla\overrightarrow{v^T}\right)\right]+\rho\vec{g}+\vec{F} \tag{7}$$

where, the static pressure is *P*, $\vec{F}$ is added force, the gravitational force is $\rho\vec{g}$, μ is viscosity**.** When simulating wave production, a piston type wave generator is employed. The properties of the waves are determined by the left wall motion function. The displacement of piston is calculated with *h* (water depth), *S* (piston displacement), *H* (wave height), $k = 2\pi / L$ (wave number). The piston displacement equation is [15]:

$$\left(\frac{H}{S}\right)_{piston}=\frac{2\left(\cosh\left(2kh\right)-1\right)}{\sinh\left(2kh\right)2kh} \tag{8}$$

Because the equation is time dependent, any wave elevation must be represented in terms of the piston's motion. When the maximum wave height value is taken as the *A* value for wave amplitude, the *S* displacement of the piston can be represented as maximum S_0. Piston displacement owing to wave period equation [16]:

$$X(t)=\frac{S_0}{2}\left(1-e^{-\frac{5t}{2T}}\right)\sin(\omega t) \tag{9}$$

The derivative of Equation 9 is the wall velocity depend on time. Equation 10 is used while the preparation of UDF. Equation 10 is [17]:

$$V(t)=\left(\frac{s_0}{2}\right)\left(1-e^{-\frac{5t}{2T}}\right)\omega\cos(\omega t)+\frac{5}{2T}e^{-\frac{5t}{2T}}\sin(wt) \tag{10}$$

2.3. Fluent setup selection

The aim of this paper briefly explains the NWT analysis, so the user interface options of the CFD program Fluid Flow (Fluent) module are defined in Table 2 and Table 3. Before running the calculation, the selection of "Adapt > Region" is done. In this selection air and water volumes are defined by using the "Mark" button after initialization of the solution. Then "Patch…" button is used for defining the water phase (phase-2 must be chosen under the "Phase" heading) Volume Fraction Value. If the defined volume which is chosen under the heading "Register to Patch" is assumed full with air the value under heading "Value" is 0. When defining water volume this value of volume fraction becomes 1. After this procedure patch button is used to close the window. All the options are settled as shown in Table 2 and Table 3 before running the calculation.

Table 2. Solution setup in fluent flow (fluent) setup section

Solution Setup		
General	Solver	*Type > Pressure-Based* *Velocity Formulation > Absolute* *Time > Transient* *2D Space > Planar*
	Gravity	*Z (m/s) = -9.81*
Models	Multiphase – *Volume of Fluid* Viscous – *Realizable k-e, Scalable Wall Fn*	
Materials	Fluid	*water-liquid* *air*
Phases	Phase 1 *(air)*, Phase 2 *(water-liquid)*	
Cell Conditions	Zone *(surface_body), mixture, fluid*	
Boundary Conditions	Left, right and bottom lines = *wall*, top line = *pressure-outlet*	
Dynamic Mesh	Layering	Dynamic Mesh Zones > Left wall – *Rigid Body*

Table 3. Solution in fluent flow (fluent) setup section

Solution		
Solution Method	PISO	Gradient = *Least Square Cell Based* Pressure = *PRESTO!* Volume Fraction = *Geo-Reconstruct* Other options = *Second Order Upwind*
Solution Initialization	Hybrid	(Adapt phases then) *Patch…* (Regions)
Calculation Activities	Automatic Export	*CFD-Post Compatible*
Run Calculation	Time Step Size (s) <= *0.005* Max Iterations/Time Step => *45*	

2.4. User defined function

The UDF is written in the C programming language and introduced in the Fluent module of the program. The dynamic variables in the system are defined in the program to obtain the wave.

The first UDF code must be defined in the Fluent Setup section. The buttons used for this operation is “Define > User-Defined > Functions > Complied…” and then Source Files “Add…” button is used to add the file of c code, Header Files “Add…” button is used to add libraries “udf.h” and “dynamesh_tools.h” which are in the folder of Fluent > libudf > src. The header libraries are written in beginning of C code with first line “ #include "udf.h" ” and second line “ #include "dynamesh_tools.h" ”.

The third line of the code is header as "DEFINE_CG_MOTION(wave,dt,vel,omega,time,dtime)". The variables used in code must be defined in brackets near of header. The function code is “ 4{ Thread *t; 5face_t f; 6t = DT_THREAD(dt); 7float T,S; 8begin_f_loop(f,t) 9{vel[0] = …}end_f_loop(f,t) } “. T is period of wave and S is displacement of wall in the code. “vel[0] = …” is the velocity in the x direction of wave maker which can be seen in Equation 9. When code is written, the assumption of is made in programming.

In Fluent Setup Section, the dynamic mesh structure used during wave generation is chosen as "Layering". “Dynamic Mesh > Create/Edit…” button is used to select left wall as “Dynamic Mesh Zone”. The function which is compiled is chosen under the header option of “Motion/UDF Profile” is chosen motion as “Rigid Body”. The object is separated into small squares in this mesh structure. Each square is separated by 0.1 m on one side. These sections can be separated from one another within the mesh framework. On moving mesh structures, the program is used to solve the effects of gravity on water particles.

3. Results

When analyses are performed, the geometry of the NWT is not changed. The heights of the generated wave, wave period, height and depth of water in various different situations are compared with each other by varying results. Wave characteristics and positioning of the conditions are shown in Table 4.

While the instances are being determined and simulated, the NWT is 200 meters long. The results are reviewed once comparisons are made between the cases. In some circumstances, the wave velocity varies.

Table 4. Cases and parameters

	Wave Height H(m)	Water Depth h(m)	Wave Length L(m)	Wave Period T(s)
Case 1	1	16	53.6	6
Case 2	2	16	53.6	6
Case 3	2	28	56	6
Case 4	2	16	25	4
Case 5	2	5.11	53.6	8

3.1. Validation

Numerical studies' dependability is determined by comparing them to experimental, analytical, or other results published in the literature. In the aforementioned work, an NWT simulation with a water depth of 16 m at the start and a tank length of 200 m was employed for validation. A-line 20 meters from the NWT's left edge is used for sampling. The value of the water depth variable on a line can be obtained from the Fluent Results Section. An expression is defined in the Results section. For example if “Line 1” is the name of the line from which the water height results are obtained and “Phase 2” is

the volume fraction of water, the expression for water depth variable becomes "lengthInt(Phase 2.Volume Fraction)@Line 1". The chart of expression versus time gives the transient water depth values on a line.

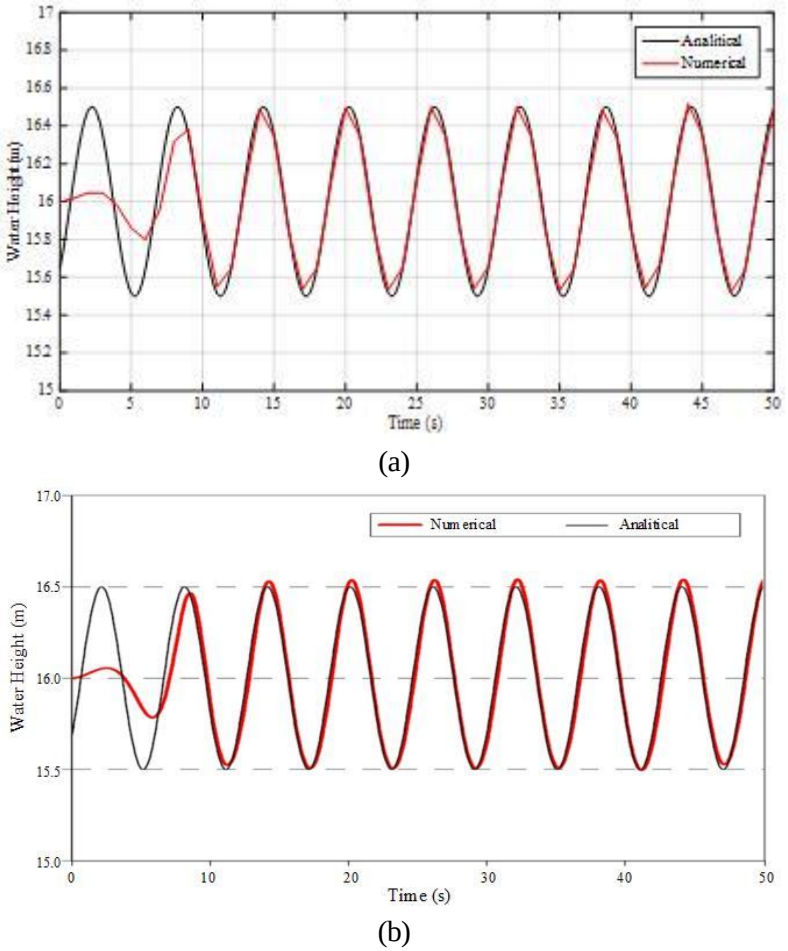

Figure 2. Validations (a) this study (b) study of gomes et al. [18].

A water surface level change vs. time chart is given. The created wave has a period of 6 seconds and a height of 1 meter. In Figure 2b, the study by Gomes et al. [18] is used for validation, in this work, Figure 2a depicts an analytical and numerical (time-dependent) water-time chart of water height. This analytical value is calculated from the basic sinusoidal wave equation. Wave height versus time charts can be seen in Figure 2.

3.2. Wave generation results

The movement of gas and liquid phases depends on time can be seen in Figure 3. The red component represents water with a volume fraction of 1, the blue part represents air with a volume fraction of 0, and there is an isosurface line connecting the two parts. The isosurface volume fraction is approved at 0.5. The color difference between portions indicates that the mesh structure contains a mixture of water and air. The variability of the volume fraction from 0 to 1 can be seen using contours. The tank's right wall is considered to be fixed. There's no such thing as a damping function or a porous structure. Because the right wall of the pool lacks a dampening function, the length of the pool is significantly more than the depth of the water, preventing errors near the left wall. This decreases the likelihood of measurement errors near the left wall. Figure 3 shows waves with identical amplitudes are formed at areas near of left wall of the NWT.

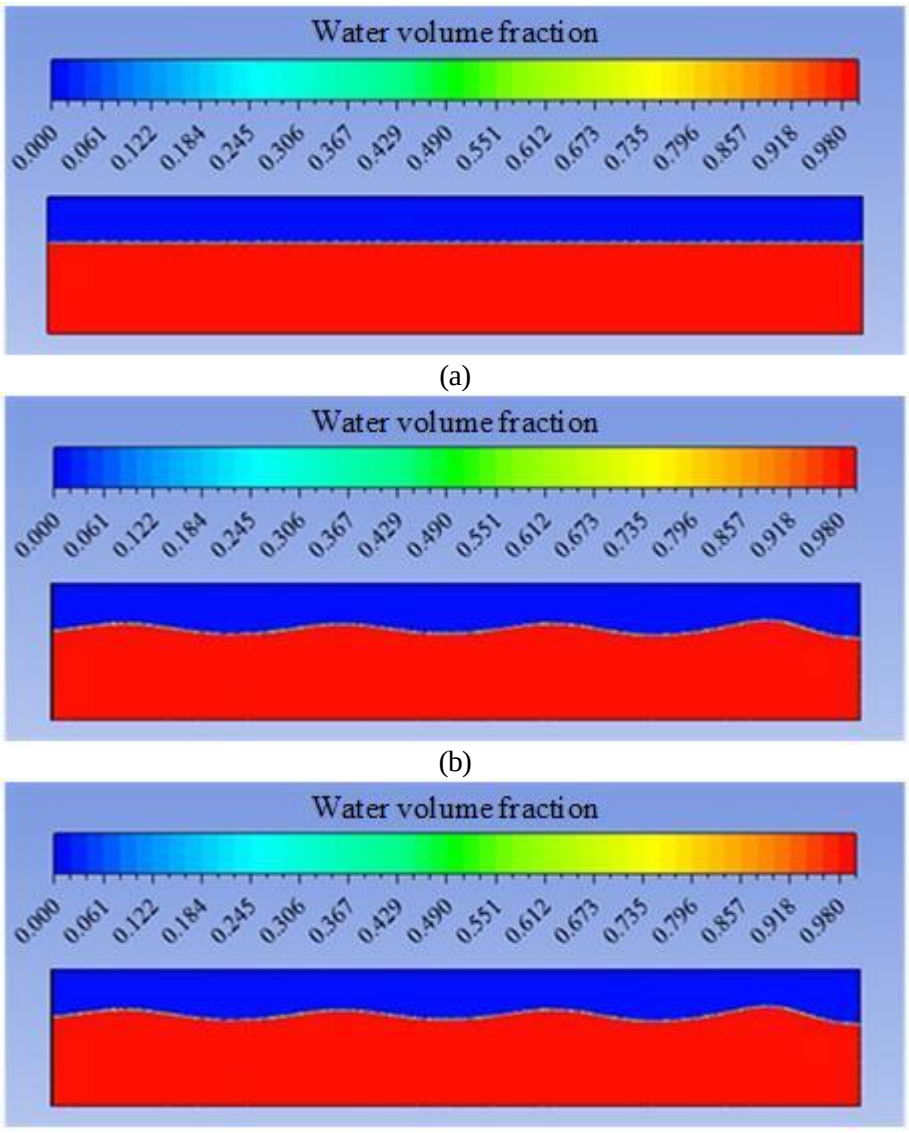

Figure 3. Water volume fractions in case 2 as represent all Cases (a) t = 0 s (b) t = 25 s (c) t = 50 s

Figure 4 shows the velocities in the x-direction for the second case. At the start, all of the velocities are 0. In the transient solution, the velocities indicate differences by time up to the end of the tank. The negative velocities are caused by the left wall's negative x-direction movement, which is influenced by UDF. Wave theory works best with negative velocities. Negative velocities in the x-direction related to dynamic water surface boundary conditions are caused by the elliptical motion of water particles. As it approaches wave trough, the negative x velocity increases, while the positive x velocity increases.

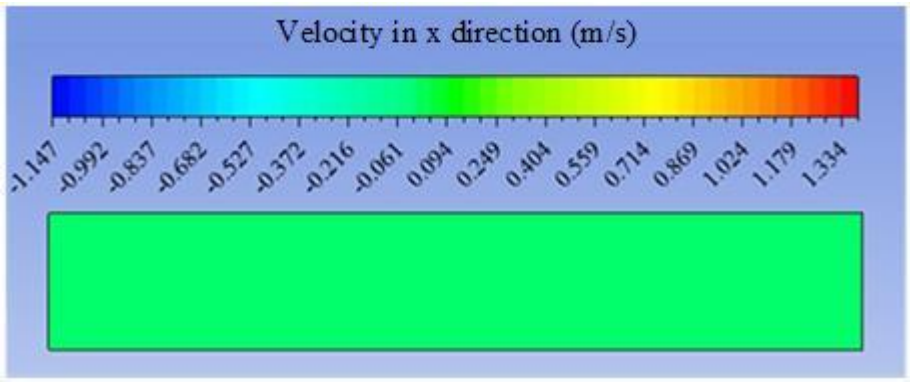

(a)

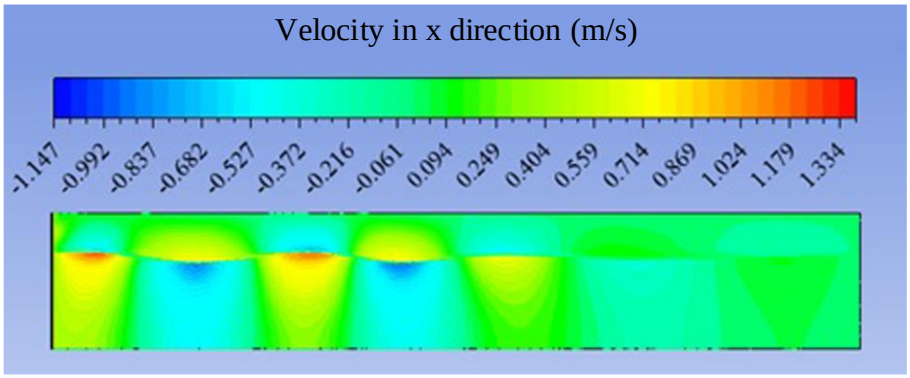

(b)

Figure 4. *u* velocity in second case of numerical wave tank (a) t = 0 s (b) t = 25 s

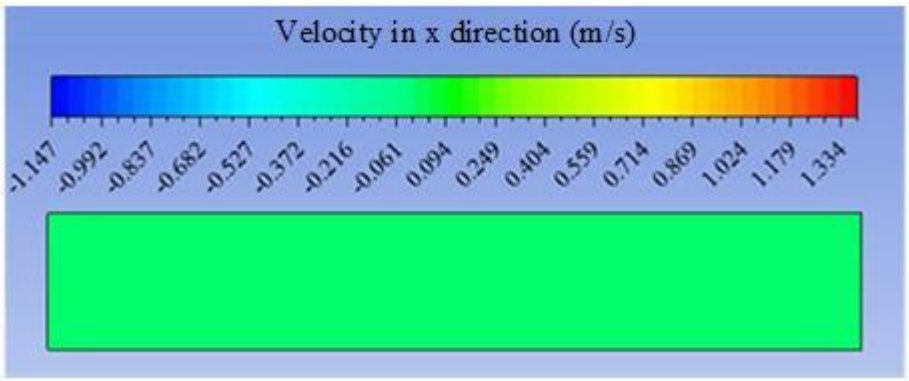

(a)

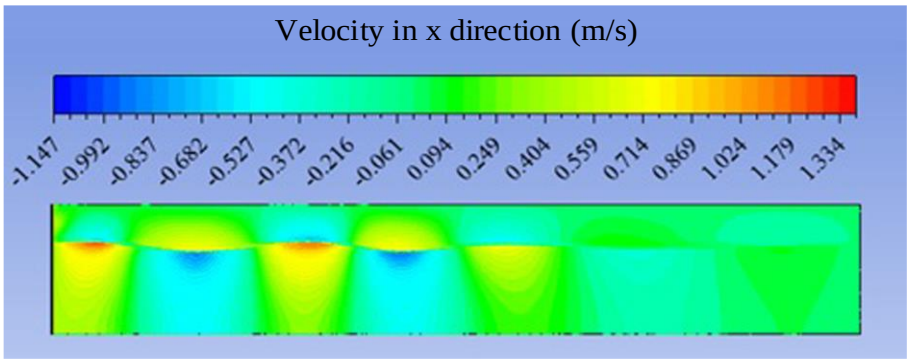

(b)

Figure 5. *v* velocity in second case of numerical wave tank (a) t = 0 s (b) t = 25 s

Figure 5 shows the velocities in y-direction for the second case representing all of the cases in the numerical study. The variable values of u velocities cause differences in pressure and momentum forces based on Navier-Stokes Equations. At the crests and troughs of waves, pressure fluctuations are greatest.

Figure 6 shows the dynamic pressure values in the NWT. Dynamic pressure values are directly related to velocities. For Case 1 the wave height is 1 m, while for Case 2 it is 2 m. As a result, the dynamic pressure value reaches values close to 4 times of Case 1 in Case 2.

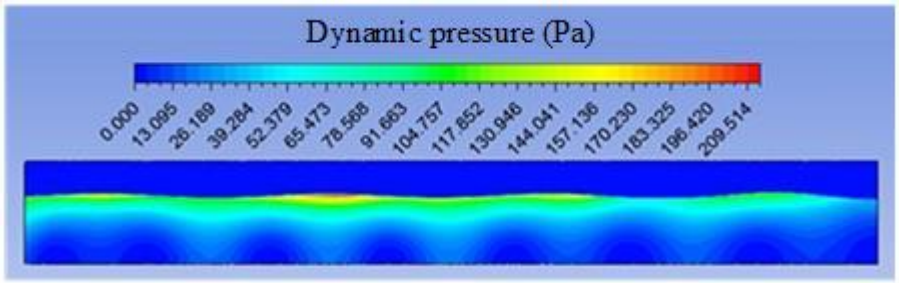

(a)

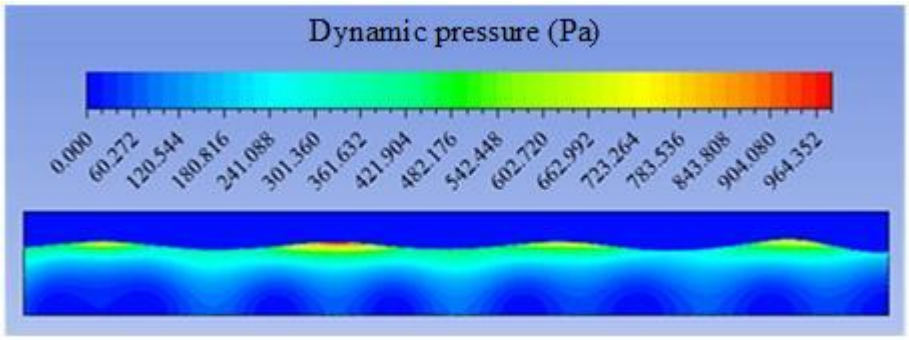

(b)

Figure 6. Dynamic pressures of time = 30 s (a) first case (b) second case

The comparison of Case 1 and Case 2 for observing the differences in results due to wave elevation also has implications for other cases. Figure 7 shows turbulent kinetic energy values. For Case 2, these values are several times higher than Case 1. This result also indicates that the amount of energy to be produced is excessive. Because, in principle, electric energy is the transformed state of the kinetic energy of the waves. Kinetic energy has higher values due to higher wave height. As the water particle movement decreases towards the depth of the water, the highest kinetic energy values are approached in the wave forming regions. Kinetic energy formation is also observed in the gas phase due to the liquid phase movement. Since the contours contain the mass ratio of the kinetic energy, the colors above and below the droplet are the same, but the kinetic energy of the liquid phase is considerably higher than that of the gas phase.

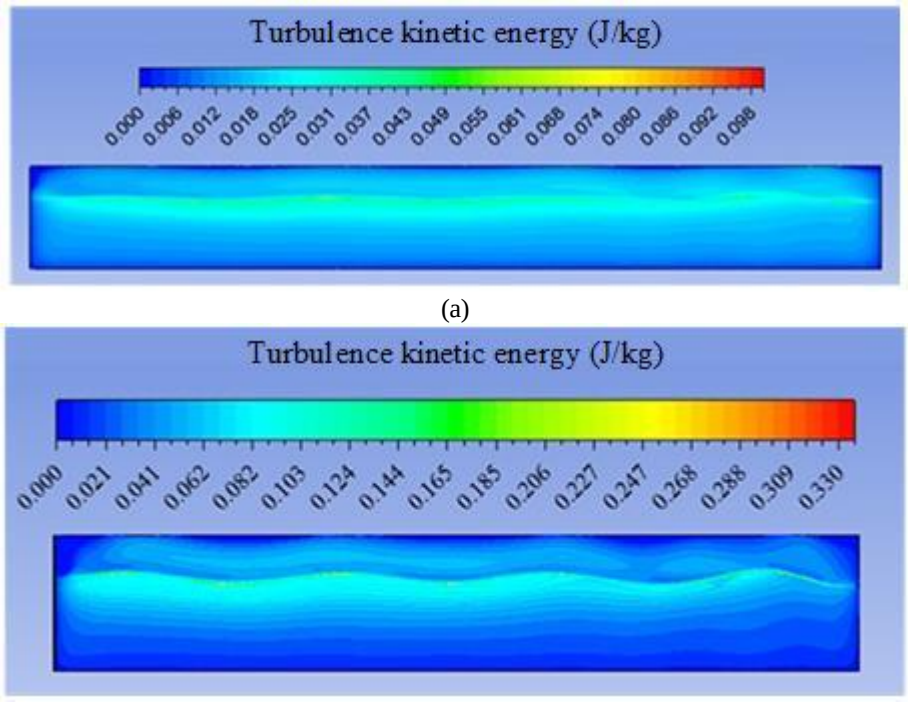

Figure 7. The turbulent kinetic energy of time = 30 s (a) first case (b) second case

The absolute pressure value of Case 4 is shown in Figure 8. Determining the pressure output shows the correctness of the simulated case where the area is colored equal to the open-air pressure.

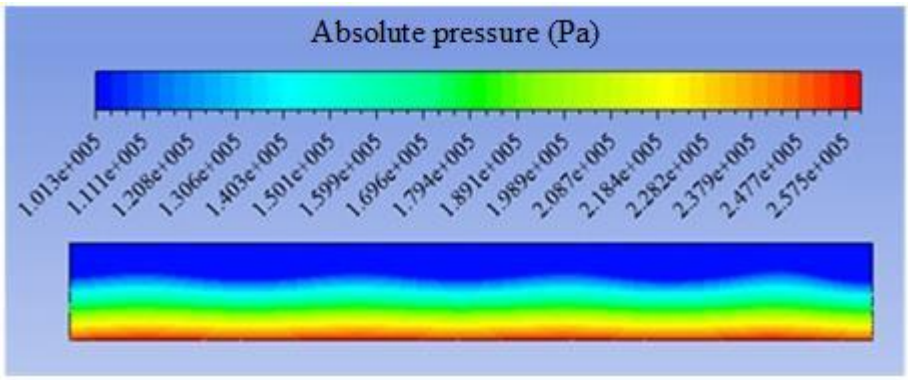

Figure 8. Absolute pressure at t = 50 s in case 4

All results and figures are evidence of the movement in the NWT. The results can be used in calculations of the effect of the waves on solids or energy converters.

4. Conclusion

In the study, NWT simulations are carried out and the determining characteristics are modeled with time-dependent waves. The numerical study's findings are compared to the analytical findings. The NWT simulations were generated with the methods used to give appropriate results for gravity waves. Since the water depth wavelength ratio affects the results, this should be taken into account during the simulation work. The volume fraction, velocity profiles and pressure values can be clearly observed in the 2D NWT. The processes during generating waves are explained briefly.

NWT studies form the basis for further studies to determine the effect of the fluid on the solid surface in the future. Wave energy conversion systems with stationary, floating or moving systems to be defined in the fluid, behavior analysis of floating objects, the effect of fluid movement in the water can be examined. As a result, it is expected that this work will generate new work and can be utilized as a source for studies on the subject.

5. Author Contribution Statement

In the study, Author 1 contributed to the analysis of the results, provision of the materials and examination of the results; Author 2 contributed to forming the idea, making the design and literature review; Author 3 contributed to checking the spelling and checking the article in terms of content.

6. Ethics Committee Approval and Conflict of Interest

There is no need for an ethics committee approval in the prepared article. There is no conflict of interest with any person/institution in the prepared article.

7. References

[1] Agamloh EB, Wallace AK, von Jouanne A. "Application of fluid-structure interaction simulation of an ocean wave energy extraction device". *Renewable Energy*, 33(4), 748–757, 2008.
[2] Liang B, Wu G, Liu F, Fan H, Li H. "Numerical study of wave transmission over double submerged breakwaters using non-hydrostatic wave model". *Oceanologia*, 57(4), 308–317, 2015.
[3] Finnegan W, Goggins J. "Linear irregular wave generation in a numerical wave tank". *Applied Ocean Research*, 52, 188–200, 2015.
[4] Bhinder MA, Babarit A, Gentaz L, Ferrant P. "Potential time domain model with viscous correction and CFD analysis of a generic surging floating wave energy converter". *International Journal of Marine Energy*, 10, 70–96, 2015.
[5] Yao Y, Chen Y, Zhou H, Yang H. "Numerical modeling of current loads on a net cage considering fluid–structure interaction". *Journal of Fluids and Structures*, 62, 350–366, 2016.
[6] Liaghat T, Guibault F, Allenbach L, Nennemann B. "Two-way fluid-structure coupling in vibration and damping analysis of an oscillating hydrofoil". *ASME International Mechanical Engineering Congress and Exposition Proceedings*, Huston, Texas, USA, 1-13, 9-15 November 2015.
[7] Liu Z, Hyun BS, Hong KY. "Application of numerical wave tank to OWC air chamber for wave energy conversion". Proceedings *Eighteenth International Offshore and Polar Engineering Conference*, Canada, 350–356, July 2008.
[8] Wang BL, Liu H. "Higher order Boussinesq-type equations for water waves on uneven bottom". *Applied Mathematics and Mechanics*, 26(6), 774–784, 2005.
[9] Zhu Y, Li Y, Tao A, Zhang J. "Numerical modeling of wave interaction with double curtain-wall breakwater". *Procedia Engineering*, 116(1), 1009–1018, 2015.
[10] Ojieh NC, Barltrop NDP, Xu L. "RANS investigation of the kinematics of an alternative extreme wave". *Ocean Engineering*, 36(17-18), 1415–1424, 2009.
[11] Liang X, Yang J, Li J, Li X. "A numerical study on local characteristics of predetermined irregular wave trains". *Ocean Engineering*, 38(4), 651–657, 2011.
[12] McCormick ME. "*Ocean engineering wave mechanics*". John Wiley & Sons Inc, 1973.
[13] *ANSYS Fluent Theory Guide 15.0*. ANSYS, Inc.
[14] Versteeg HK, Malalasekara W. "*An introduction to computational fluid dynamics the finite volume method*". London: Longman Group, 1995.
[15] Dean RG, Dalrymple RA. *Water Wave Mechanics for Engineers and Scientists*, 2. World Scientific, 1991.
[16] Liu Z, Hyun B, Jin J. "Numerical analysis of wave field in owc chamber using VOF model". *Journal of Ocean Engineering and Technology*, 22(2), 1-6, 2008.
[17] Gomes MN, Isoldi LA, Olinto CR, Rocha LAO, Souza JA. "Computational modeling of a regular wave tank". *Journal of Thermal Engineering*, 8(1), 44–50, 2009.
[18] Gomes MN, Isoldi LA, Olinto CR, Rocha LAO, Souza JA. "Computational modeling of a regular wave tank". *Proc. - 2009 3rd South. Conf. Comput. Model. MCSUL*, 60–65, 2009.